Technische Universität München
Fakultät für Physik

Abschlussarbeit im Bachelorstudiengang Physik

Spatial Momentum Correlations within a Universal Particle Emission Source in pp Collisions at the LHC

Impuls und Ort Korrelationen innerhalb einer universellen Partikelemissionsquelle in pp Kollisionen am LHC

Jaime González González

31. Juli 2022

Erstgutachter (Themensteller): Prof. Dr. L. Fabbietti
Zweitgutachter: Prof. Dr. J. Friedrich

Abstract

This work introduces a new powerful framework (CECA) to model the source function that represents the spatial and kinematic properties of a particle emission in small collision systems like proton–proton and proton–lambda. The properties of the source have been fixed within CECA by using an existing ALICE measurement of the p–p source size in p–p collisions. Under the assumption of a common source, a simulation of the kinematic properties of the p–Λ system is performed and compared to existing measurements. Due to a disagreement, the assumption is further explored by modeling the p–Λ interaction with different parametrizations of the state of the art model, the chiral effective field theory, and fitting the main observable, the correlation function. The result of this work is the conclusion that a weaker interaction for the two-body force of the p–Λ system is required to accommodate the assumption within the framework. This conclusion could, if proven right, further constrain the p–Λ interaction and give further insight into the inner structure of neutron stars.

Contents

Chapter 1

Introduction

The strong force acts on very small scales (c.a. $1\ \mathrm{fm} = 10^{-15}\ \mathrm{m}$), yet, due to its strength, binds the protons and neutrons (nucleons (N)) together, allowing the existence of the matter that we perceive throughout our universe. The fundamental underlying theory is that of quantum chromodynamics (QCD), which describes the interaction between quarks mediated by gluons. The gluon self coupling and the large coupling constant α_S are unique features of QCD, making the theory non-perturbative at low energies. There are effective models attempting to provide the necessary tools to study the strong interaction, where the chiral effective field theory (χEFT) is the state of the art [1, 2]. The chiral model concentrates only on the observable bound states of quarks and gluons, called hadrons. A hadron composed of a quark and an anti-quark is called a meson, while bound states of three quarks, such as the nucleons, are called baryons. The lightest meson is the pion (π), and within the χEFT it is used as an effective mediator of the strong force.

In general, the strong force is relevant only under extreme densities, thus it is rarely observed on a macroscopic scale. However, a notable exception are neutron stars, the remnants of collapsed massive supergiant stars and the densest stellar objects known in our universe. With masses of one to two times the solar mass $\mathrm{M}_\odot$ and radii of around 10 km, the densities of these astronomical bodies exceed that of regular nuclear matter ($\rho_0 = 0.15\ \mathrm{fm}^{-3}$). These conditions lead to several interesting theoretical possibilities, for example hyperons (Y), baryons with at least one strange quark, may be produced, and even deconfinement of quarks might be possible [3]. Although the density and, therefore, the pressure in the core of a neutron star is immense, it remains stable due to the interplay between the fermion pressure of the baryons and the gravitational pull. The relation of density to pressure is described by the nuclear equation of state (EoS) and combined with the Tolman-Oppenheimer-Volkoff (TOV) equation, a mass–radius relation for stellar bodies can be established. However, the EoS is determined by the microscopic properties of the composing matter, in particular the strong force acting between the particles. In this way a connection between the microscopic and macroscopic parts of the universe is realized, and the strong interaction is key to understanding it. Nevertheless, our experimental knowledge is mostly limited to scattering experiments involving nucleons, and nuclear effects at density of ρ_0. This is insufficient for the study of neutrons stars, due to the possible existence of hyperons at larger densities. Consequently, the theoretical predictions are not well constrained and vary drastically. An example of several prediction for the EoS and the corresponding mass–radius relation of a neutron star is shown in Fig. 1.1. An interesting paradox, called the "Hyperon puzzle", is the experimentally

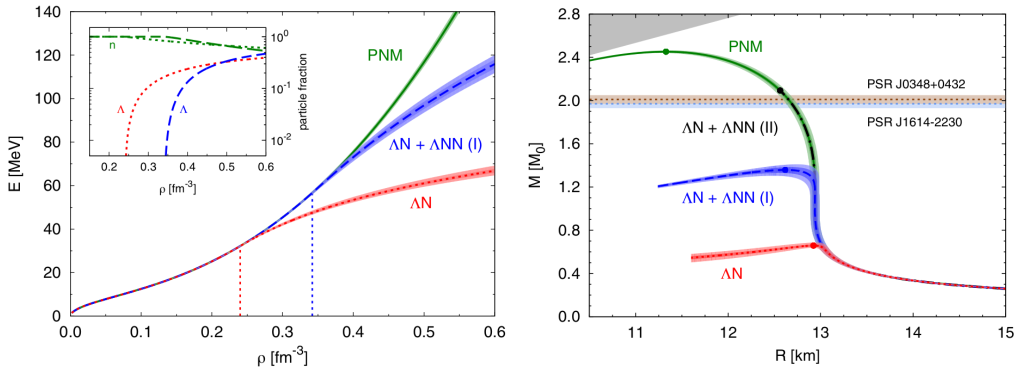

Figure 1.1: [4] Nuclear equation of state. The green line defines the case of pure neutron matter, the red line includes Λs considering only the two-body NΛ interaction and the blue line accounts for the three-body force in addition. The black dashed line contains a non-physical strength of the three-body force. The left panel shows the EoS, the right panel the corresponding mass–radius relation for NSs. The horizontal line at 2 $\mathrm{M}_\odot$ corresponds to several measurements of NS masses; any realistic EoS needs to reach this line.

confirmed existence of neutron stars with masses above two solar masses, which stands in contradiction with a *soft* EoS accommodating an attractive $\mathrm{p}\Lambda$ interaction. The latter is confirmed by scattering experiments, thus there are certainly missing physics effects to resolve the contradiction. Further, the density dependence of the interaction is model dependent, and the three-body interactions could provide further repulsion. This calls for dedicated experimental work to address these open questions.

In this work the focus is on the femtoscopy technique, which has recently been proven a powerful tool to access the strong interaction [5, 6]. This is achieved by means of measuring correlations between particles produced at collider experiments. As will become evident in the rest of this chapter, the femtoscopy formalism heavily relies on the particle emission after the collision, which has to be accurately modeled in order to investigate the final state interaction (FSI) [7]. The present thesis deals primarily with the modelling of the particle emission. The study is extended within the context of the $\mathrm{p}\Lambda$ two-body interaction and the test of χEFT.

Femtoscopy

Based on the "Hanbury Brown and Twiss effect" [8, 9], in which the intensity fluctuations of stellar bodies are correlated to their spatial dimensions, femtoscopy is the study of the momentum correlations between particles and the association to their wave functions [10]. In astronomy, it is achieved through an independent intensity measurement of a light signal, split and diverted into two different detectors. Under the assumption of a coherent emission time, a correlation between the two intensities should appear due to the spatial distribution of the light-emitting source. In collider experiments, this method can be applied to the subatomic scale, although some modifications are necessary. The observables needed are the yield of particles, which replaces the intensity, and the spatial point of their formation (hadronization). The region where the latter takes place is described by an effective emission source.

Femtoscopy has been initially used to study identical pion $(\pi - \pi)$ correlations, in order to test and verify quantum statistical effects [11]. The development of a theoretical description, driven by the Lednický-Lyuboshitz (LL) model, provided the possibility of probing correlations by accounting, in an approximate way, for the Coulomb and strong force [12]. Femtoscopy studies would later be performed in heavy-ion collisions, at the Relativistic Heavy Ion Collider (RHIC), to test the hydrodynamic models used to model the supposedly created quark-gluon plasma [10]. This was accomplished by investigating the size of the emission source through measuring the correlation function of identical pions, making use of their quantum statistics.

In the last several years femtoscopy has been used in a non-traditional way, where the interaction between particles has been studied under the assumption of a known emission profile. This has been achieved using the ALICE detector at the Large Hadron Collider (LHC), where a dedicated analysis has been performed in proton–proton (pp) collisions [7], demonstrating that such small collision systems have two main benefits. First, the small size of the emission source (1 fm) is comparable with the range of the strong force, leading to a large correlation signal. Second, the emission source has been proven to be identical for protons and Λ hyperons, allowing the assumption of a common source function for all baryons. Consequently, the emission can be studied by using the correlations between particle pairs of known interaction, such as a pair of protons, and fix the source function for any particle pair of unknown interaction. In this way correlation studies can probe the FSI with high precision, leading to many interesting results [5–7, 13–20]. The listed analyses performed by ALICE relied on the "Correlation Analysis tool using the Schrödinger equation" (CATS) [21], which allows the inclusion of any interaction and emission profile without the approximations within the LL model. However, an accurate modelling of the emission region is essential for the study of the interaction; there is, unfortunately, still a lack of solid understanding on the properties of the emission function, apart from a pioneering work performed by the

ALICE collaboration [7] that resulted in the development of the Resonance Source Model (RSM).

Within the present thesis, I have worked alongside my supervisor Dimitar Mihaylov on an extension of the RSM, named "Common Emission in CATS" (CECA), that is more generic and allows to account for spacial-momentum correlations during the emission. This is essential to reproduce certain observables linked to the collective expansion of the collision system, such as the dependence of the source size on the transverse momentum ($\mathrm{k_T}$) and mass ($\mathrm{m_T}$) of the emitted particles. The goal has been to anchor the source parameters within CECA to the known p–p source, and make prediction for the p–Λ emission profile. Finally, the source size and its $\mathrm{m_T}$ dependence have been compared to the measured ALICE data. A small inconsistency has been observed, thus the measured correlation functions have been re-analyzed using several different parameterizations of the p–Λ interaction within the χEFT model. Under the assumption of the common source within CECA, it has been found that a slightly lower strength of the two-body p–Λ force in vacuum provides a better description of the ALICE data. While the results are not yet conclusive, this finding may be one of the missing pieces needed for solving the "Hyperon puzzle". This work sets the roadmap for future related experimental and theoretical studies.

Chapter 2

The femtoscopy method

2.1 The correlation function

The correlation function $C(k^*)$ of two particles offers an approach to study the underlying subatomic interaction and the processes that lead to the particle emission. It is the main observable in femtoscopy and is evaluated as a function of the relative momentum of the pair

$$\mathbf{k}^* = \frac{1}{2} \cdot (\mathbf{p}_2^* - \mathbf{p}_1^*) \,, \tag{2.1}$$

where $\mathbf{p}_{1,2}^*$ are the single particle momenta, and the asterisk denotes the pair rest frame (PRF). The correlation function is sensitive to the properties of the emission source $S(\mathbf{r}^*)$, where $\mathbf{r}^*$ is the relative distance between the particles, and the wave function $\Psi(k^*, \mathbf{r}^*)$ of the pair. The work of M. A. Lisa, S. Pratt, R. Soltz and U. Wiedemann [10] offers a summary of the field and an insight into heavy-ion collisions. It also provides the means to construct the **Koonin-Pratt equation**, which is extremely important as it relates the experimentally observable correlation function to both $S(\mathbf{r}^*)$ and $\Psi(k^*, \mathbf{r}^*)$.

$$C(k^*) = \frac{P(\mathbf{p}_1^*, \mathbf{p}_2^*)}{P(\mathbf{p}_1^*)P(\mathbf{p}_2^*)} = 1 + \int S(\mathbf{r}^*) \left[\left| \Psi(\mathbf{k}^*, \mathbf{r}^*) \right|^2 - 1 \right] d^3r^* \tag{2.2}$$

The free wave function is by convention normalized to 1 since it corresponds to no interaction, therefore, the integral in Eq. 2.2 becomes 0. This in turn means that the correlation function will be equal to 1. The first part of Eq. 2.2 is related to the statistical definition of the two-particle correlation function. It is given as the ratio of the probability $P(\mathbf{p}_1, \mathbf{p}_2)$ to find, at the same time, a particle with momentum $\mathbf{p}_1$ and a second with $\mathbf{p}_2$ to the product of the individual probabilities $P(\mathbf{p}_1)P(\mathbf{p}_2)$. These probabilities can be expressed in terms of the corresponding differential yields $N_{1,2}$, resulting in:

$$C_{\text{stat}}(\mathbf{p}_1, \mathbf{p}_2) = \frac{\langle P(\mathbf{p}_1, \mathbf{p}_2) \rangle}{\langle P(\mathbf{p}_1) \rangle \langle P(\mathbf{p}_2) \rangle} = \frac{dN_{1,2}/(d^3p_1 \cdot d^3p_2)}{(dN_1/d^3p_1) \cdot (dN_2/d^3p_2)} \tag{2.3}$$

This ratio will equate to one in absence of any correlation, which is consistent with the convention used by Koonin-Pratt. Experimentally, the correlation function is expressed using the second part of Eq. 2.3, i.e. the yields of the particles. To be consistent with definition 2.2, $C_{\text{stat}}(\mathbf{p}_1, \mathbf{p}_2)$ is projected onto k^*, leading to

$$C_{\text{exp}}(k^*) = \mathcal{N}\frac{N_{\text{same}}(k^*)}{N_{\text{mix}}(k^*)}. \tag{2.4}$$

The numerator, $N_{\text{same}}(k^*)$, corresponds to the case of two correlated particles, while the denominator $N_{\text{mix}}(k^*)$ is a reference sample composed of pairs that did not experience any final state interaction. Experimentally it is possible to construct both. The so called "same event" sample $N_{\text{same}}(k^*)$ is the yield of two particles of relative momentum k^* that were measured within the same collision (event), while the "mixed event" sample $N_{\text{mix}}(k^*)$ is obtained by combining together particles produced in different events [5]. Further, Eq. 2.4 contains a normalization factor $\mathcal{N}$, which is used to normalize the correlation function at large k^*. The femtoscopic signal is typically located below 200 MeV/c, for this reason the normalization can be applied, as long as $C(k^*)$ becomes flat, outside of this region. Nevertheless, the actual physics embedded in the correlation function is related to the its shape; the normalization constant is, therefore, often irrelevant to the final result. As will be explained later, this is connected to the non-femtoscopic signals within the measured correlation, which are typically fitted to the data and result in a non-flat baseline that absorbs any normalization effects.

The right side of Equation 2.2 can be rewritten as

$$C_{\text{th}}(k^*) = \int S(r^*)\left|\Psi(\mathbf{k}^*, \mathbf{r}^*)\right|^2 d^3r^*. \tag{2.5}$$

This form represents the purely theoretical definition of the correlation function, and considers the source function as a probability density that only depends on the magnitude of r^*. It will be important to separate, throughout this work, between $C_{\text{th}}(k^*)$ and $C_{\text{exp}}(k^*)$, since the latter contains many effects that come on top of the theoretical definition. These will be discussed in the current section and will be accounted for in the analysis.

Equation 2.5 can be simplified even further by assuming a radially symmetric source function. Employing spherical coordinates to integrate over d^3r^* will result in a factor of 4π from the angular components. Consequently, the Koonin-Pratt equation is reduced to the one dimensional integral

$$C_{\text{th}}(k^*) = \int_0^\infty S_{4\pi}(r^*)\left|\Psi(\mathbf{k}^*, \mathbf{r}^*)\right|^2 dr^*, \tag{2.6}$$

where

$$S_{4\pi}(r^*) = 4\pi r^{*2} S(r^*). \tag{2.7}$$

The emission and the interaction are usually studied separately due to the loss of differential information through the integration over the radial component. For that reason, in order to study the source function, a system of known interaction has to be measured. The "standard candle" in the present work is the p–p correlation, because the interaction is very well constrained by scattering experiments and can be accurately modeled by the Argonne $\nu18$ potential [22]. By contrast, the p–Λ interaction is known with a lower precision, thus any model predictions, in this work exclusively given by χEFT, have to be treated under the consideration of large systematic biases. Figure 2.1 shows examples of the p–p and p–Λ correlation functions (circles), measured by the ALICE collaboration [7], with the corresponding fit functions (colored bands), obtained from $C_{\text{th}}(k^*)$, and applied necessary corrections. As discussed, both correlations become flat

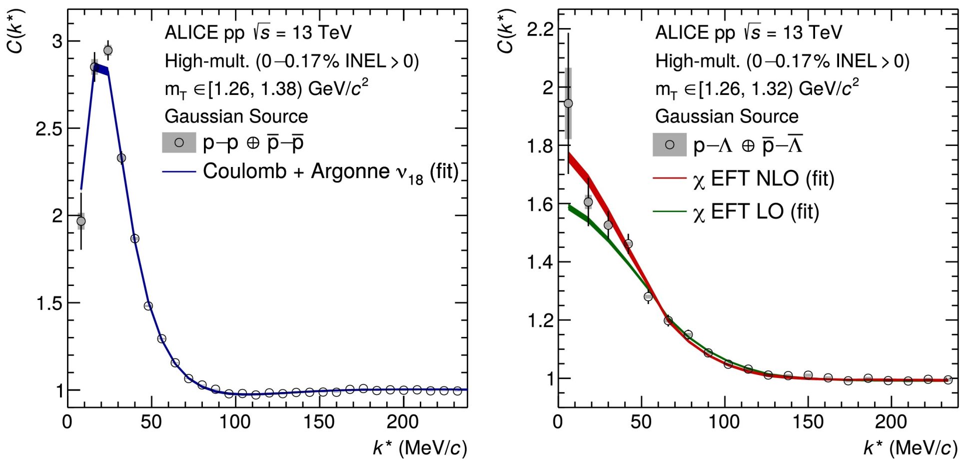

Figure 2.1: [7] Exemplary correlation function of p-p (left), obtained by using the Argonne ν_{18} [22] potential, and p-Λ (right), using χEFT LO [23] and χEFT NLO [2] potentials.

and converge towards unity above 200 MeV/c, while a clear femtoscopic signal is present at lower momenta. In this particular case the emission source has been assumed to have a Gaussian profile

$$S(r^*) = \frac{1}{(4\pi r_0^2)^{3/2}} \exp\left(-\frac{r^{*2}}{4r_0^2}\right), \tag{2.8}$$

with source sizes of 1.28 fm for p–p and 1.41 fm for p–Λ. The corresponding probability density functions (PDFs) for $S_{4\pi}(r^*)$ are shown in Fig. 2.2. These distributions peak at around 2.5 fm, thus the bulk of the correlation signal is linked to the value of the wave function at this distance from the scattering center. The strong force acts on a comparable scale, therefore, it is expected to find particles closer together for an attractive interaction and further apart for a repulsive. The overall enhancement of both correlations in Fig. 2.1 is a manifestation of the attractive nature of the strong force for both of these pairs. The p–Λ system is composed of non-identical particles with the Λ being neutral in charge, thus the only contributing factor to the correlation is the

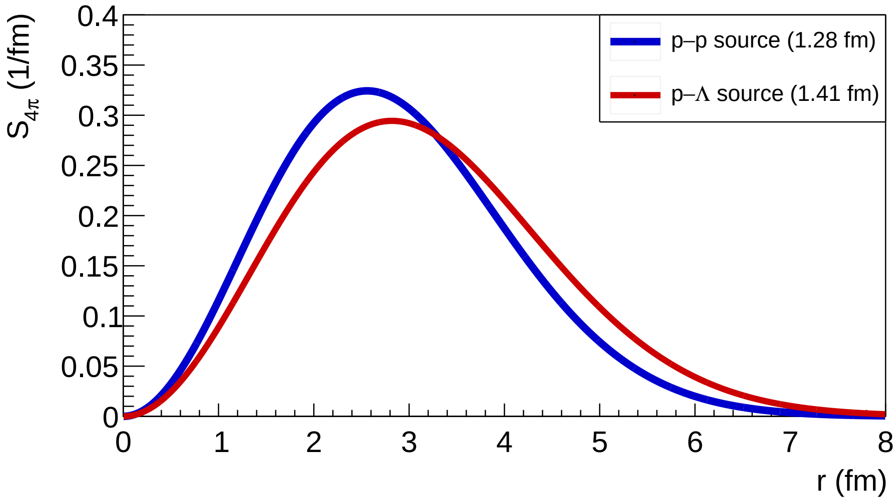

Figure 2.2: The Gaussian source used to fit the p–p and p–Λ correlations shown in Fig. 2.1.

strong force. Consequently, the correlation function has a monotonic rising behaviour as $k^* \to 0$ is approached. However, p–p is a system of identical particles, subject to Pauli blocking (quantum statistics), and consists of two positively charged particles, which will experience a repulsive Coulomb force. These two effects lead to a depletion of the correlation function, counteracting the enhancement due the strong interaction. The repulsive contribution becomes dominant at low k^* and manifest itself, in $C(k^*)$, as a peak at around $20\,\text{MeV}/c$, whence it decreases toward lower k^*. The broadness of the quantum statistic term is known to be inversely proportional to the source size, therefore, the width in a small collision system will be

$$\sim \hbar c/r_0 = \frac{197\ \text{MeV} \cdot \text{fm}}{1.28\ \text{fm}} \approx 154\ \text{MeV},$$

which is partially the reason for the slight dip within $C(k^*)$ visible between 100 and 150 MeV/c in the left panel of Fig. 2.1.

The generic ideas presented before will be discussed in further detail in the subsequent sections. In particular:

- Section 2.2: Experimental effects
- Section 2.3: Modelling the interaction
- Section 2.4: Modelling the source

2.2 Experimental effects

The experimental effects are outside the scope of the current work, however a brief summary will be presented. For a detailed discussion the following sources are available: [5, 24].

Momentum resolution

The most trivial experimental effect is due to the finite momentum resolution. It is present for any detector, and leads to a smearing of the correlation function. For the ALICE experiment the effect is in the order of 4 MeV/c in k^*, and is quantified with the help of full scale Monte-Carlo simulations. The information extracted from the simulations is the smearing matrix $M(k^*_{\text{true}}, k^*)$, which quantifies how the true relative momentum is transformed into k^*. This affects the measured yields ($N(k^*)$) of the same- and mixed-event sample.

$$N_{\text{measured}}(k^*) = \int_0^{\infty} M(k^*_{\text{true}}, k^*) N_{\text{true}}(k^*_{\text{true}}) dk^*_{\text{true}} \tag{2.9}$$

There are two approaches to account for the effect of the momentum resolution. The first one is to apply the effect on $C_{\text{th}}(k^*)$ and the second is to unfold the same- and mixed-event distributions. The latter is generally more difficult to perform, but has the benefit of transforming the measured correlation to an experimentally unbiased state. In the work of the ALICE collaboration [7], related to the study of the source, the first approach was used, as will be in the present work.

Decomposition of the correlation function

The identification of genuine primary particles in collider experiments is susceptible to false contributions from misidentified particles and feed-down additions from decay products of other primary particles. For example, if a fraction of the measured protons are misidentified pions, the same fraction of the experimental p–Λ correlation function will be linked to the π–Λ interaction. An exemplary case of a feed-down would be producing two primary Λs in the event, that interact. Eventually they will decay ($c\tau = 7.89$ cm) into a proton and a pion, and in most cases the decay products are detected and, based on their invariant mass, a Λ candidate is reconstructed. Nevertheless, it may happen that one of the decay protons is wrongly assigned to be a primary particle, in which case it will enter the p–Λ correlation function. The detected signal will be linked to the original Λ–Λ interaction, modified due to the decay kinematics. There are standard methods to account for these effects [5], in which the fraction λ_i and correlation signal $C_i(k^*)$ of each non-genuine contribution i are evaluated. The correlation function breaks down into a genuine (C_{gen}) and a residual part.

$$C_{tot}(k^*) = 1 + \lambda_{gen} \cdot [C_{gen}(k^*) - 1] + \sum_i \lambda_i [C_i(k^*) - 1] \tag{2.10}$$

Non-femtoscopic correlations

Another effect that skews the correlation function is the non-femtoscopic background, which mainly affects the region of large relative momentum above 200 MeV/c. These may be related to a multitude of effects, such as conservation laws or a correlated emission, and are very difficult, in many cases practically impossible, to model. Since they are expected to have a reasonably smooth behaviour at low momenta, it is possible to parameterize them by a polynomial function, which is then multiplied with the correlation function. The parameters of this polynomial are determined by fitting the data in a region outside the femtoscopic signal. An additional constrain may be imposed by demanding a zero derivative at $k^* = 0$ for the non-femtoscopic signal, which is typically the case for any type of correlation due to the disappearing phase space of both, the same- and mixed-event samples. A solid choice of a background baseline (BL) function is a polynomial of third degree, which has a zero linear term [20].

$$C_{BL}(k^*) = a + b \cdot {k^*}^2 + c \cdot {k^*}^3 \tag{2.11}$$

Considering all experimental effects, the function which can be used to model the data is

$$C_{model}(k^*) = C_{BL}(k^*) \cdot C_{tot}(k^*) \tag{2.12}$$

where, depending on the analysis, the momentum resolution effects needs to be included in $C_{tot}(k^*)$. Note that if Eq. 2.12 is used to fit an experiment function $C_{exp}(k^*)$ and all baseline parameters in Eq. 2.11 are left free, the normalization constant $\mathcal{N}$ becomes obsolete.

2.3 Modelling the interaction

Based on the Koonin-Pratt relation (Eq. 2.6), one of the components needed to evaluate the correlation function, genuine or otherwise, is the wave function of the studied pair. One straight forward approach is adopted by the Lednický-Lyuboshitz (LL) analytical model [12]. It provides the means to describe the correlation function by simplifying the analytical treatment of the wave function. It relies on the assumption of an isotropic source with a Gaussian profile (Eq. 2.8) and a computation of the wave function in the asymptotic region. The outgoing function of a scattered wave on a potential can be expressed as a free wave and a scattered spherical wave with the scattering amplitude $f(\theta)$ [25], which describes the probability of scattering in any given direction θ.

$$\Psi(\mathbf{k},\mathbf{r}) \approx e^{-i\mathbf{k}\cdot\mathbf{r}} + f(\theta)\frac{e^{ikr}}{r} \tag{2.13}$$

The effective range expansion is applied on the scattering amplitude and the result is a function of the momentum that takes in two parameters, the scattering length f_0 and the effective range d_0.

$$f(k) \approx \left(\frac{1}{f_0} + \frac{1}{2}d_0k^2 - ik\right)^{-1} \tag{2.14}$$

Combining these two expressions with the Koonin-Pratt equation (Eq. 2.6) brings forth the **Lednický-Lyuboshitz equation**, an expression that is analytically solvable for a Gaussian source of width r_0.

$$\begin{aligned} C_{LL}(k^*) = 1 + \frac{1}{2}\left|\frac{f(k^*)}{r_0}\right|^2 \left(1 - \frac{d_0}{2\sqrt{\pi}r_0}\right) \\ + \frac{2\,\mathrm{Re}[f(k^*)]F_1(2k^*r_0)}{\sqrt{\pi}r_0} - \frac{\mathrm{Im}[f(k^*)]F_2(2k^*r_0)}{r_0}, \end{aligned} \tag{2.15}$$

where $\mathrm{Re}[f]$ and $\mathrm{Im}[f]$ denote the real and imaginary part of the complex scattering amplitude. F_1 and F_2 are analytical functions that result from the approximation with a Gaussian source. Since the wave function is derived based on its phase-shifted asymptotic form, it will not be accurate at small distances for non-zero potential. For the strong interaction this corresponds to several femtometers. The bracketed term in Eq. 2.15 is partially correcting the shape of the wave function at low distances, nevertheless, the correction is sensible only for $d_0 < r_0$, thus the LL model remains difficult to apply for very small source sizes; such is the case in pp collisions. The form of the LL presented above is only valid for non-identical particle in the absence of Coulomb interaction, although both of these effects can be accounted for by further extending the formalism [24].

CATS framework

A different approach to study the correlation function is to compute the two-particle wave function exactly. This can be accomplished by employing the "Correlation Analysis Tool using the Schrödinger equation" (CATS) [21], which solves the Schrödinger equation numerically. The solution will be accurate at any distance, which means that there is no limitation on the source size for which the framework can be applied. Any analytical or non-analytical function can be used as an input to the source, as the integral in Eq. 2.6 is evaluated numerically. The only current limitation of the framework is that the interaction potential has to be real, and means that it is applicable to purely elastic scattering.

Nevertheless, externally evaluated wave functions can be passed into CATS, even if they have imaginary terms, to evaluate the Koonin-Pratt integral. This allows to use the output of sophisticated models, such as χEFT, as direct input for CATS to evaluate $C(k^*)$ for any desired source function.

Another benefit of the CATS framework is the ability to apply all experimental corrections, described in section 2.2, on top of the genuine correlation, enabling the evaluation of the "model" correlation (Eq. 2.12).

2.4 Modelling the source

The source distribution reflects the probability to emit a pair of particles at a distance r^* in their rest frame. In the case of an uncorrelated pair emission, which is typically assumed in femtoscopy, the source function can be derived from the single particle emission distributions. These are described in good approximation by a Gaussian of width r_0 for each spatial (Cartesian) coordinate. This ansatz leads to Eq. 2.8, which corresponds to the two-particle Gaussian source. Figure 2.3 compares the functional shape of sources with varying sizes, found in collider experiments. The typical size in pp collisions is ~ 1 fm, while heavy-ion systems have an r_0 parameter of at least 5 fm. For comparison, the strong potential has a range of c.a. 2 fm, thus smaller collision systems have the advantage of probing the non-asymptotic part of the interaction. Apart from the independent particle emission, this simple derivation does not account for Lorentz boost effects, nor for anisotropic emission. Further, non-Gaussian effects, e.g. production of particles through (exponential) decays, are not taken into account. The latter has been claimed to be a dominant effect in small collision systems, and has been thoroughly investigated by the ALICE collaboration [7]. It has been demonstrated that p–p and p–Λ pairs exhibit a difference in their source sizes of c.a. 15%. This can be seen in the left panel of Fig. 2.4. Here, the source size r_0 has been plotted as a function of the **transverse mass** of the pair (m_T).

$$m_T{}^{1} = \sqrt{k_T{}^2 + m^2}, \tag{2.16}$$

where m is the average mass of the particle pair and k_T the average transverse momentum. The transverse mass scaling is attributed to the collective expansion of the system [10]. This prompted the ALICE collaboration to develop the "Resonance Source Model" (RSM[2]), which accounted for particle production through intermediate short lived (~fm/c) resonances. These decay before they develop a strong FSI signal with the surrounding particles, thus their effective contribution is a small exponential shift of the emission point of their daughters. The typical example is a Δ resonance decaying

[1]This definition of m_T is approximate and only applicable for particles of low k^*.
[2]Details are provided later in this section.

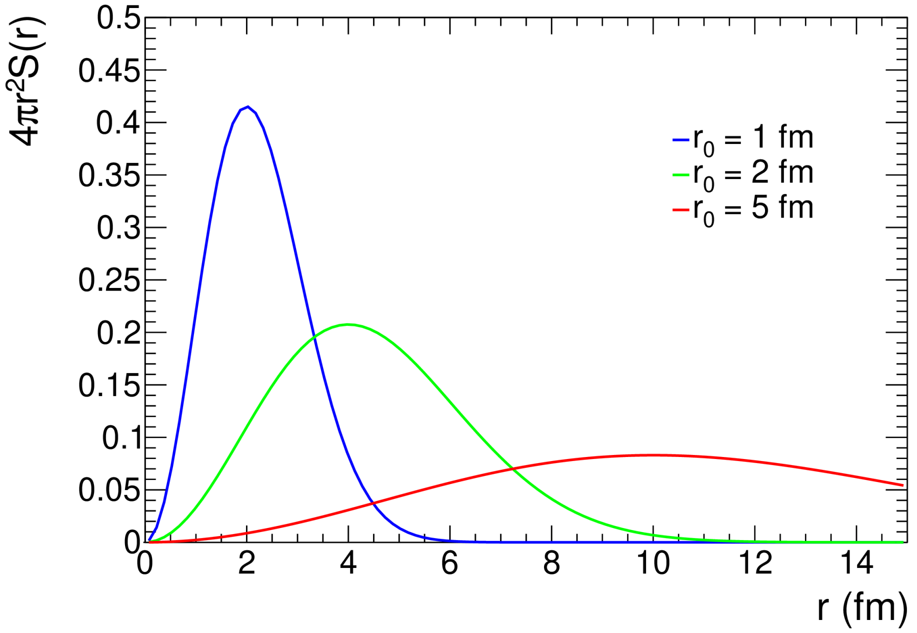

Figure 2.3: Examples of the source function, times the angular term of the integration $4\pi r^2$, for different sizes.

into a proton and a pion. The RSM uses a simple numerical procedure, performed within the pair rest frame, to propagate the initial (primordial) resonances until they decay, and the spatial coordinates of their daughters shape the source function. The input parameters are the size r_{core} of the Gaussian core source of the primordials, their kinematic properties and relative abundances. The plots in the right panel of Fig. 2.4 are obtained by treating r_{core} as a free fit parameter, with the kinematics fixed from the EPOS transport model [26] and the particle abundances extracted from the statistical hadronization model (SHM) [27]. After re-fitting the p–p and p–Λ correlation functions in each m_T bin, the resulting r_{core} is found to be identical.

The observation of a common core source in p–p and p–Λ has been seen as a great success, and widely used in following analyses to fix the source function in order to study pairs of unknown interaction [5–7, 13–20]. The recipe has been to measure the average m_T of the studied pair, and extract the corresponding value of r_{core} from the pp result shown in Fig. 2.4. Nevertheless, apart from the explicit treatment of the resonances, the other possible modifications of the source have not been accounted for. For example, there are no Lorentz boost effect, and the m_T scaling is not intrinsically in the RSM, due to the lack of collective effects. The m_T scaling seen in Fig. 2.4 is obtained by

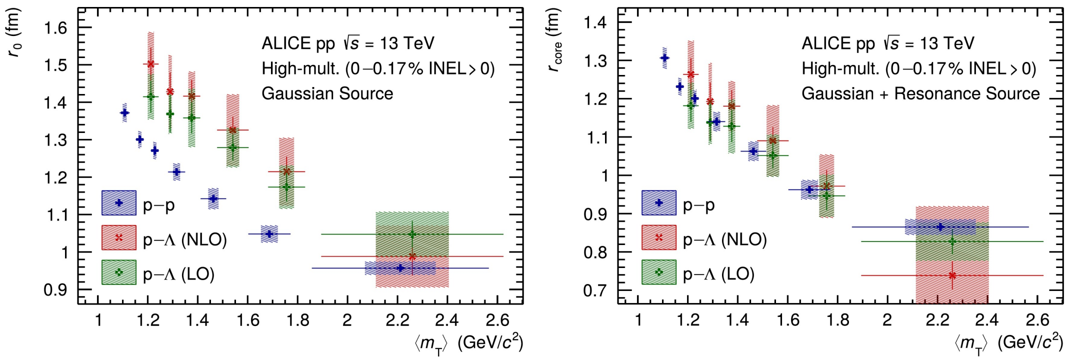

Figure 2.4: [7] Source radius r_0 (left) as a function of the transverse mass $\langle m_T \rangle$, obtained from fitting the correlation function as shown in figure (2.1). Accounting for resonances with the RSM yields a core source radius r_{core} as seen on the right.

fitting each m_T bin individually, but the m_T itself is *not* a parameter of the RSM model. These are the challenges set to be addressed by the new model CECA. This thesis is performed as part of the development program for CECA, where the model has been compared to ALICE data. Details on CECA are provided in chapter 3, and details on the corresponding data analysis in chapter 4.

Details on the Resonance Source Model (RSM)

The goal of the RSM is accounting for the origin of the particles. Many stable particles of interest, such as protons, are the decay products of resonances, and their lifetime affect the source function. Long lived resonances ($c\tau \gtrsim 10$ fm) that travel further than the size of the source can be left out, since the FSI already occurred between the primordial particles. On the other hand, shorter lived resonances need to be taken into consideration. Their decay lengths are of the same order as the source size, which leads to a very short FSI between the primordials. In this case, the experimentally observed particles, where at least one of them is a daughter of a primordial resonances, do not only carry the correlations related to their interaction, but also inherit the ones between the primordial particles. However, the latter can be neglected due to the very short time of the decays, simplifying the problem. This implies that the correlation signal is the result of the interaction of the measured (daughter) particles only. The resonance source model (RSM) was introduced to quantify the effect of strongly decaying resonances, and confirm the common baryon source [7].

For the accurate description of the effects of resonances, it is necessary to know the fraction of primordial particles. This information can be obtained with the help of the statistical hadronization model (SHM) and for both protons and Λs it amounts to $\approx 36\,\%$

[7, 27], which means that resonances are the dominant production mechanism and their effect cannot be ignored. There are numerous resonances feeding into both protons and Λs, therefore, to simplify the computation, the RSM works with the yield averaged mass and lifetime of all relevant resonances. The same approach will be adopted in the present analysis using CECA. For protons (Λs) these are $< \mathrm{M}_{\mathrm{reso}} >= 1.37$ GeV/c^2 (1.46 GeV/c^2) and $< \tau >= 1.65$ fm/c (4.69 fm/c). The lifetime of the resonances feeding into Λ particles is larger, therefore, the observed apparent source size r_0 (left panel in Fig. 2.4) is also larger. Figure 2.5 shows how the RSM works schematically. An initial

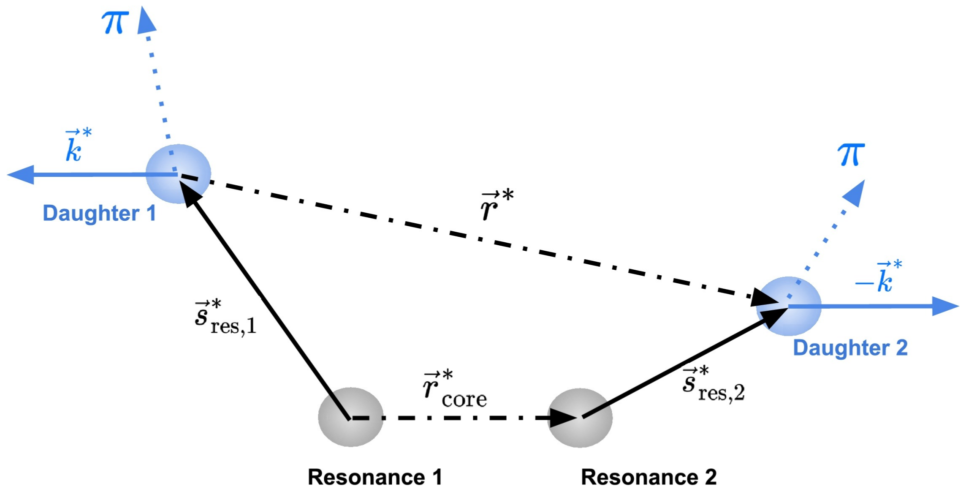

Figure 2.5: [7] Illustration of primordial particles (gray), which correspond to the core source function with a radius of $\vec{\mathrm{r}}^*_{\mathrm{core}}$, decaying into particles of interest (blue) and generating an effective width $\vec{\mathrm{r}}^*$ of the source function.

distance $\mathrm{r}^*_{\mathrm{core}}$ is generated randomly following a Gaussian distribution (Eq. 2.8), then the primordial particles, in case they are resonances, are propagated on a straight line based on their momenta. The momentum vectors are not known and need to be sampled from a realistic transport model. The default choice for the RSM has been EPOS [26]. Next, the resonances decay and the daughters form the final pair of interest. It may be, of course, that a pair is formed from one primordial particle and a daughter of a decay product. This would correspond to setting $\mathbf{s}^*_{\mathrm{res},1}$ or $\mathbf{s}^*_{\mathrm{res},2}$ to zero (Fig. 2.5). The relative distance between the daughters $\mathrm{r}^* = |\mathbf{r}^*|$ is saved in a histogram to build up the corresponding source distribution. All quantities are evaluated in the rest frame of the daughters. A comparison between the core source and the modified p–p and p–Λ sources is shown in Fig. 2.6, where a very pronounced exponential tail can be seen and deviates from the Gaussian profile at large r^*. Further details on the procedure and the results can be read in the PhD thesis of Dimitar Mihaylov [21] and the dedicated ALICE paper [7].

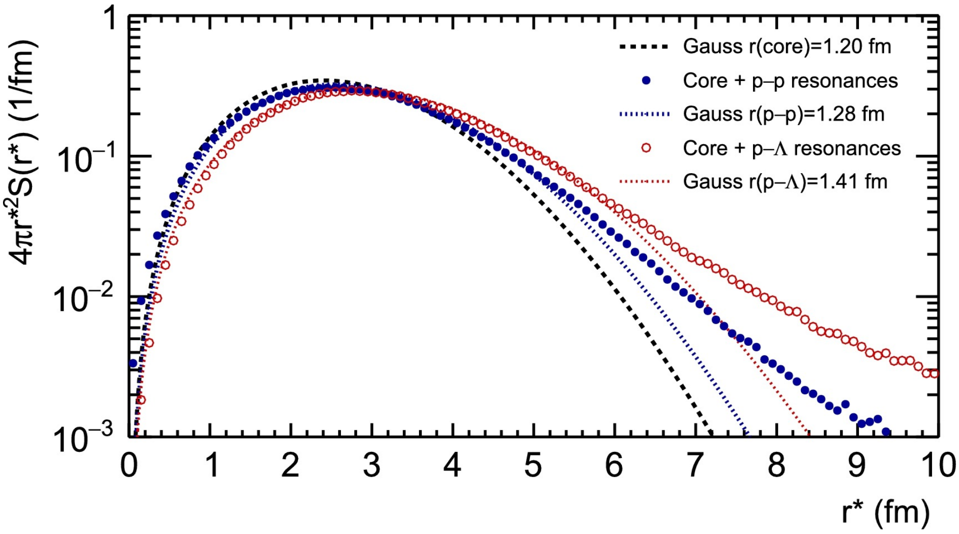

Figure 2.6: [7] Source function distributions (circles) fitted with a Gaussian profile (colored dotted lines) to extract the width. The exponential tail shows the effect of the resonances for protons and Λs. The core distribution (black dashed line) is identical for both p–p and p–Λ.

Chapter 3

Common Emission with CATS

A new tool, developed in C++, for the modeling of the source is the **Common Emission with CATS** (CECA). It is an improved and more generic framework than the RSM, that uses single particle distributions to generate the source. The RSM delivered great results and many analyses were performed based on this model, but it had several limitations, as discussed in section 2.4, which necessitated an upgrade.

The first step for CECA to work is the definition of a particle database containing the properties of the simulated species. This includes their relative abundances, momenta distributions and masses. Additionally, the lifetimes and decay channels, including the branching ratios, are needed if short-lived resonances contribute to the production of the studied species. With this in place, CECA generates a pool of random particles from which only those relevant to the analysis are saved. This includes not only the particles of interest, but also those that are required for the chain decays, from which the studied species may be produced. The simulation is performed in terms of events, in which a fixed number of particles are generated. The species of each particle is chosen randomly, based on the provided abundances. The momenta are sampled from the corresponding single particle distributions. While this takes care of the kinematics, a more detailed modeling is required for the spatial properties at the time of the hadronization. All particles initially start with a zero space and time component. The final point of emission is determined by several input parameters. Although this aspect of the model is still in development, three of the parameters, alongside their generic concepts, will be introduced and investigated in the present work. In particular:

- **The displacement point ($\mathrm{r_d}$):** a random Gaussian distributed displacement around the collision point, which corresponds to the origin of the coordinate system, that can be individually set for any spatial axis. If this parameter is used alone for the modeling of the emission, and boost effects are neglected, it is equivalent to the definition of the two-body source described with Eq. 2.8. Alternatively, if used in conjunction with other parameters, it can be understood as a fluctuation in the emission point, which is related to the inner structure of the hadron.
- **The hadronization length ($\mathrm{r_{hl}}$):** this parameter defines the surface of an ellipsoid located around the displacement point. It can be controlled in each individual spa-

tial direction. This parameter is inspired from Heavy–Ion collisions, and represents the overall geometric shape of the expanding system, which deviates from a perfect sphere. Subsequently, the momentum vector, that has been sampled from the corresponding momentum distribution, and its intersection point with the surface defines the hadronization. In case no further parameters are used, it would also be the point of emission. So far the time component remains zero, however the "clock" of the particle is now activated in the laboratory (LAB) frame of reference.

- **The time offset (τ_{off}):** This parameter is a constant, corresponding to the amount of time needed for the effective emission to occur after the hadronization process. The time offset can be treated as a "proper time" for each particle, which is the default choice, or as a constant within the LAB. The propagation is performed on a straight line, i.e. ignoring any possible FSI, based on the velocity of the particle. After the set amount of time elapses, the position of each particle is considered the point of emission. This parameter can be controlled individually for each particle, however this case has not yet been extensively studied.

The above three parameters are treated as being common for all particles. This implies that any differences in the single particle sources are attributed to differences in the momenta/velocities of the particles. At this stage, the kinematics, spatial and time coordinates are saved. Next, the resonances are selected, propagated and decayed in the LAB frame, according to an exponential distribution based on their lifetime. This brings the single particle part of the simulation to an end, as now all species of interest have been produced. To construct the two-body source, the particles are grouped into pairs, by making all possible permutations within the event. From here, the particles are boosted into the pair's rest frame. For each pair the starting time of the interaction is decided by retrieving the value of the particle formed second. The first is propagated, again on a straight line, in order to obtain the relative spacial coordinates of the two particle at the same time. The latter is a condition required by femtoscopy [10].

The effects of these parameters on the source distribution can be demonstrated by running CECA exclusively with the individual variables. The following investigation will separate the core and total (effective) source. The core corresponds to the emission point of the primordial particles of interest, ignoring any resonances and their decays. The total source is evaluated by taking into consideration all particles of interest, regardless of their origin. After setting up CECA with an arbitrary value for the displacement parameter, the framework goes through the aforementioned processes and generates a range of histograms related to the kinematic and spatial properties of the emission. This includes, for example, the angle distributions and, more importantly, the source distribution. Since the framework saves the information of the single particles, individual observables such as the $\mathrm{m_T}$ are easy to extract for differential studies. This simulated source distribution is then fitted with the Gaussian profile (Eq. 2.8), from which the effective width of the source is extracted. This is performed for pairs of $\mathrm{k}^* < 100\,\mathrm{MeV/c}$, in order to select only

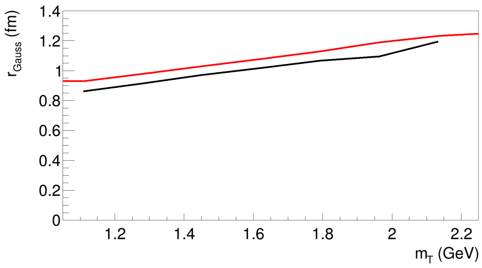

(a) Displacement of 0.8 fm

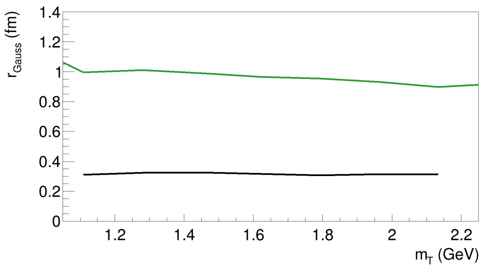

(b) Time offset of 4 fm/c

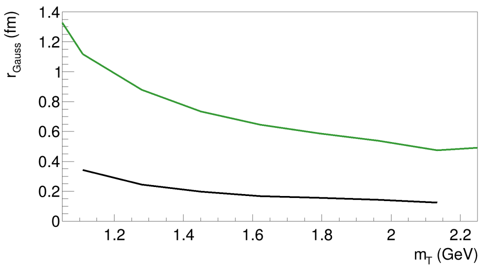

(c) Hadronization scale of 4 fm

Figure 3.1: Effect of the different parameters of CECA with a Gaussian source. The black line denotes the primordial source and the colored line the effective source size.

the candidates relevant for femtoscopy. This process will be used throughout the whole analysis performed within the scope of this work. Figure 3.1 shows the resulting relation between the source size and pair $\mathrm{m_T}$ for Boltzmann distributed momenta, and particles and resonances set to correspond to the p–p correlation, as studied by ALICE [7]. On these plots the total effective source (colored lines) and the underlying core source (black lines) of the primordial particles are shown. This helps to monitor the effect of the production through resonances. Figure 3.1 provides a lot of information, all of which will be discussed below, split into two paragraphs: one regarding the core-to-effective Gaussian size ratio and one regrading the $\mathrm{m_T}$ scaling.

Core-to-effective Gaussian size ratio

To begin with, the displacement parameter generates a scaling with an upward slope shown in Fig. 3.1a, whose effective size does not increase much compared to the core. The change is about 10$\%$, which seems low given the comparable source size[1] and lifetime (c.a. 1.7 fm) of the resonances. However, this can be explained by the completely

[1]A 1 fm Gaussian source size correponds to roughly 2 fm average separation between the particles (Fig. 2.3).

random orientation of the spatial and momentum vectors, which leads to a sizeable probability for the resonances to move toward the center (back toward the collision point) and decay well within the volume corresponding to the primordial emission. For this reason the total source size is only marginally increased. The effect will be more pronounced for larger lifetimes of the resonances, since then the particles travelling "backwards" will decay well outside the primordial source.

The next parameter is the time offset and its effect on the core is a systematic increase in size proportional to its value. The core source function is a compact distribution while the effective is much broader; the size difference is around 0.65 fm. The very compact core ($\mathrm{r_{core}} \approx 0.35$ fm) corresponds to average distances between the primordial particles of c.a. 0.75 fm, which is actually comparable to the proton radius, thus physically possible to realize. In fact, the EPOS transport model also has a very compact primordial source, that has a mean particle separation of ~ 1 fm. The large increase of the total source is associated with the strongly correlated space and momentum coordinates, which enforce the particles to travel away from the collision point and, consequently, away from each other. The production through a decay of a resonance gives the particles more time to separate from one another, while the random momentum kick of the decay breaks the perfect collective alignment of the daughters with respect to the rest of the primordials, separating them even faster.

The hadronization length has a comparable difference in the size of the core and total sources to the time offset. Similarly, the reason is the collective expansion of the system away from the collision point, resulting in strong space-momentum correlations.

Source dependence on the transverse mass

The arbitrary values for the plots in Fig. 3.1 were chosen to provide similar effective size of the compared sources. It is apparent that the $\mathrm{m_T}$ scaling is very different for each of the individual parameters. The data, shown in Fig. 2.4, demonstrates a source size that decreases with $\mathrm{m_T}$, however the displacement parameter represent the complete opposite trend. On the other hand, the time offset leads to an approximately flat $\mathrm{m_T}$ distribution, whereas the hadronization length generates, qualitatively, the correct shape of the scaling. In a naive picture, these relations can be explained by considering the collective behaviour of the system, related to the strong space-momentum correlations. If these are absent, particles of large $\mathrm{m_T}$ will have, on average, rather large momenta, separating them faster in the LAB. This leads to an effective increase of the source size. On the other hand, if the space and momentum coordinates are strongly correlated, two particles of large momenta (and $\mathrm{m_T}$) can only be aligned to have a small relative momentum $\mathrm{k^*}$ if they were produced very close in space. This effect may become dominant, and Fig. 3.1 shows that it is strongest under the consideration of a purely geometrical correlation between the space and momentum coordinates.

The effect of production through resonances does not show an effect on the $\mathrm{m_T}$

scaling in any of the cases, implying similar qualitative behaviour of both the core and total source. Given the different trend seen for each parameter, the $\mathrm{m_T}$ dependence observed in data is likely to be reproduced only by a combination of all three scenarios.

Chapter 4

Analysis

4.1 χEFT and the interaction potentials

To understand the analysis and the fitting procedure of the p–Λ system, it is necessary to look in more detail at the interaction. The p–Λ consists of two fermions, which can be arranged in a configuration of total spin $S = 0$ or $S = 1$. The former is called a singlet and the latter a triplet state. This reflects the 1/4 and 3/4 probability of finding the p–Λ pair in each state, which is related to the spin degeneracy [21]. In the previous ALICE analysis, related to the common source [7], the p–Λ interaction was modeled with the leading order (LO) [23] and next-to-leading order (NLO) [1] χEFT. This theory applies pseudo-scalar meson exchanges to treat the interaction in NN and YN systems, and relies on fitting to low-energy cross sections to obtain its parameters. The YN system is less constrained, since the data points from experiments are much more scarce compared to NN. For the p–Λ system the fitting is performed only on 36 data points using measurements of the cross section; an additional constraint results from hypernuclei experiments [28, 29]. In fact, there are several tunes of the chiral model, NLO13 [1] and NLO19 [2], predicting around 10% difference in the scattering length (a_t) of the s-wave triplet (3S1) channel. Both describe the existing scattering data equally well. This implies that there is not a unique solution and multiple choices are available for the parameters of the model, as well as the scattering parameters. On a positive note, this leaves room for exploring this system experimentally, which is achievable using the ALICE experiment, as demonstrated in a dedicated study [20]. In a comparison between the agreement of the different χEFT parameterizations to the p–Λ correlation function, it has been shown that the LO, with a_t $=1.23$ fm, is completely incompatible to the data, while both the NLO13 (a_t $=1.54$ fm) and NLO19 (a_t $=1.41$ fm) provide a better, yet far from satisfactory, description of the ALICE data. In particular, the NLO13 deviates by at least 4.2 standard deviations (n_σ), while NLO19 by 3.2, highlighting the possibility to further constrain the data. The NLO19 corresponds to a weaker two-body p–Λ interaction in vacuum. The chiral calculation has a non-physical cutoff parameter Λ, which has a default value of 600 MeV. The ALICE analysis reevaluates the agreement to the data for $\Lambda \in [500 - 650]$ MeV, and the best fit is achieved between 600–650 MeV. For this reason, in the present work, the default value of 600 MeV will be exclusively used.

The χEFT is considered a state of the art model to describe the YN interactions, as it works within the SU(3) symmetry and describes all related interactions. In particular, it includes the p–Σ^0 and n–Σ^+ channels, both of which *couple* to the p–Λ system. A coupled channel is described by a quantum mechanical system of different eigenstates, with the same quantum numbers, that allows the transition between the two states. E.g. a measured p–Λ pair may actually stem from the inelastic $\mathrm{N}\Sigma \rightarrow \mathrm{N}\Lambda$ process. This is a quantum mechanical effect, and as such will be visible in the wave function. The coupling effect is included in the chiral model, while the ALICE data provides sufficient precision to test it [20]. The obvious result of the coupling is a cusp structure in the p–Λ correlation function (and cross section) appearing at $\mathrm{k}^* \approx 289$ MeV/c, which corresponds to the kinematic threshold at which a N–Σ pair at rest will be seen in the p–Λ spectrum. Such a threshold exists due to the fact that the Σ has a mass of c.a. $1190\,\mathrm{MeV/c^2}$, which is larger than the Λ mass ($1116\,\mathrm{MeV/c^2}$). Nevertheless, the effect of the coupling is not only limited to the cusp, and has a slight effect on the overall shape of the correlation function, due to the interplay of all model parameters. In femtoscopy, it is often sufficient to only include the s-wave scattering, however due to the complexity of the $\mathrm{N}\Sigma \leftrightarrow \mathrm{N}\Lambda$ system it is necessary to include the d-waves as well. The p-wave scattering is not important for this particular case. The inclusion of the d-waves has been done in the most recent ALICE work on p–Λ [20], but it has *not* been included in the analysis of the source [7]. The latter made use only of the LO and NLO13 pure s-wave calculations. In this work multiple scenarios will be tested and compared.

Finally, the differences between NLO13 and NLO19 produce a change in the three-body interaction, providing further insight into neutron stars [30] and the hyperion puzzle, mentioned in the introduction. In particular, while the NLO19 has a lower two-body attraction in vacuum, it actually leads to stronger attraction in medium. Naively, this leads to a softer EoS, which is in contradiction to the measurements of heavy neutron stars. Nevertheless, a recent theoretical study shows that the three-body repulsion is expected to be stronger for NLO19 compared to NLO13 [30], and is significant enough in both cases to *stiffen* the EoS and prohibit the formation of Λ hyperons within the neutron star matter. Although, the hyperion puzzle remains unsolved, this is, at the very least, a step into the right direction. To quantify these ideas, it is necessary to study further, experimentally, both the two- and three-body interaction between hyperons and nucleons [20, 31].

4.2 CECA configuration and prediction

The first practical trial of CECA is reproducing the m_T scaling in the p–p system. This system is used as a benchmark, as the interaction is known with high precision. To achieve this, it is necessary to provide the framework with the momenta distribution of the protons, the fraction of primordial particles $P_p = 35.78\%$ and their average lifetime (1.65 fm) [7]. The distribution is taken from experimental data from ALICE and the fraction is obtained from the SHM [7, 24, 32]. The proton and Λ p_T distributions are shown in the Appendix (Figs. A.1 and A.2), while the pseudorapidity (η) is assumed flat within the ALICE acceptance range of $|\eta| < 0.8$. With these parameters set, a fine tuning of the model's source parameters is needed, with the goal of reproducing the p–p effective radius $r_0(m_T)$ (blue points in the left panel of Fig. 2.4). However, as a first step the trivial case of a Gaussian source has to be examined, to confirm the compatibility between RSM and CECA. For that, an arbitrary $r_{core} = 1.0$ fm is selected, and both core and p–p effective sources are simulated using the two models. Within CECA the displacement parameter (single particle Gaussian) is assumed identical to r_{core}, which is the case for an independent emission. An issue, related to the input parameters of the two approaches, is that the RSM uses the two-body kinematics obtained from EPOS, as opposed to CECA that uses the measured single particle p_T and η distributions. To make a fair comparison, at present the kinematics have been simulated with CECA using the assumption of a Boltzmann distribution of the single particles, and have been exported into RSM. In this way, the two models obtain exactly identical kinematic properties, and a direct comparison becomes possible. Another difference, which cannot be avoided, arises due to the boost from the laboratory to the pair rest frame, which is performed in CECA but not in RSM. This leads to an effective increase of r_{core} by 14%, for the current setup, as can be seen in Fig. 4.1. The effect is similar for p–Λ, thus the relative comparison of the two systems is not compromised, nevertheless, the effect will become more relevant for mesons. Finally, the effect of the resonances is compared by plotting the final source distributions, which look identical for both models (see Fig. 4.1).

Despite the slight non-Gaussian shape of the core and effective source distributions, they can still be fitted with a Gaussian profile to quantify their size. This will be done consistently throughout the following analysis and is well justified, as the mean value of the distributions, and consequently the effective Gaussian size, is the dominant parameter with regard to the shape of the correlation function. For the purpose of the present work, the second-order corrections can be ignored. It should be stressed, that these effects need to be accounted for any precision analysis, as they are likely to contribute by several percent, which is comparable or larger than the statistical uncertainties of the m_T integrated p–Λ correlation measured by ALICE [20].

In conclusion, CECA and RSM are compatible in terms of their treatment of shortly decaying resonances, however it is observed that even in a relatively heavy system, such as p–p, the boost into the pair rest frame has an effect on the core source distribution.

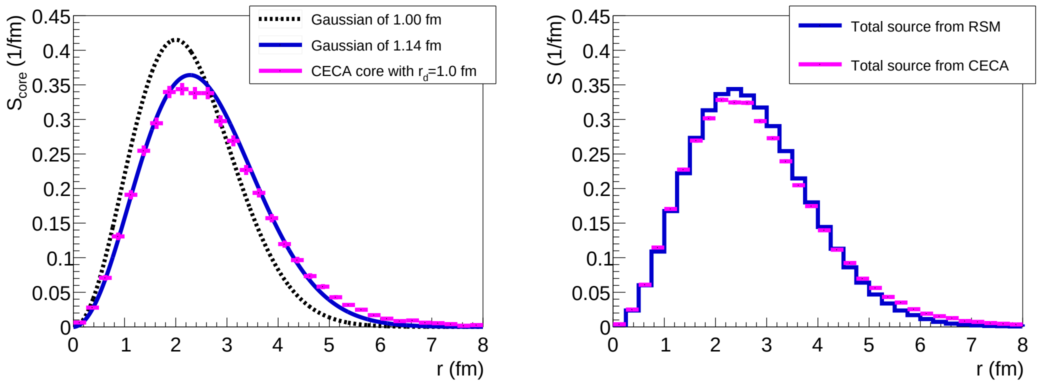

Figure 4.1: Source distributions, core in the left panel and total (including production through resonances) in the right panel, produced by RSM (blue) and CECA (magenta). The starting point is a Gaussian single particle source of 1 fm, where the corresponding two-body source is plotted with black dashed line. The size of the core in CECA is expanded to 1.14 fm, due to the transformation into the PRF. This core source has been used in RSM to produce the corresponding total source.

Since CECA is more generic it must be considered more accurate. Most importantly, it can now be used to study the m_T dependence of the source. In Fig. 4.2 the m_T scaling predicted for p–p (light-blue line), given a 1.0 fm displacement, is compared to the measured ALICE results (dark-blue points). Evidently, these two are completely incompatible, nevertheless this is not a surprise as the observed scaling is typically attributed to correlations between the spacial-momentum components at emission, which is *not* included within the random Gaussian sampling of the spacial components. In fact, similar m_T relation is observed in the EPOS transport model. It is of course possible to imitate the scaling, by fitting the m_T bins individually, with only the displacement parameter as a free fit variable, which is the equivalent to the analyses perfomed with the RSM. But this means that the m_T relation will be an artificial input, whereas the goal of CECA is to start from a single configuration and, under the assumption of a common source, predict the scaling through the introduction of spatial momentum correlations. The enforcement of these requires the introduction of additional parameters, whose combination will hopefully reproduce the correct scaling. The starting point are the relations in Figure 3.1, where the effect of the displacement r_d, hadronization length r_{hl} and time offset τ_{off} are shown. It is clear, that the displacement generates an increasing slope, whereas the required decrease can be generated using the hadronization length parameter. The time offset can be used to introduce a constant shift of the source size. With the understanding of these three parameters, it is possible to reproduce the scaling in p–p with a crude pseudo fitter. The parameters are mostly tuned by hand to find a combination that roughly mimics the measured m_T scaling, and then automatically

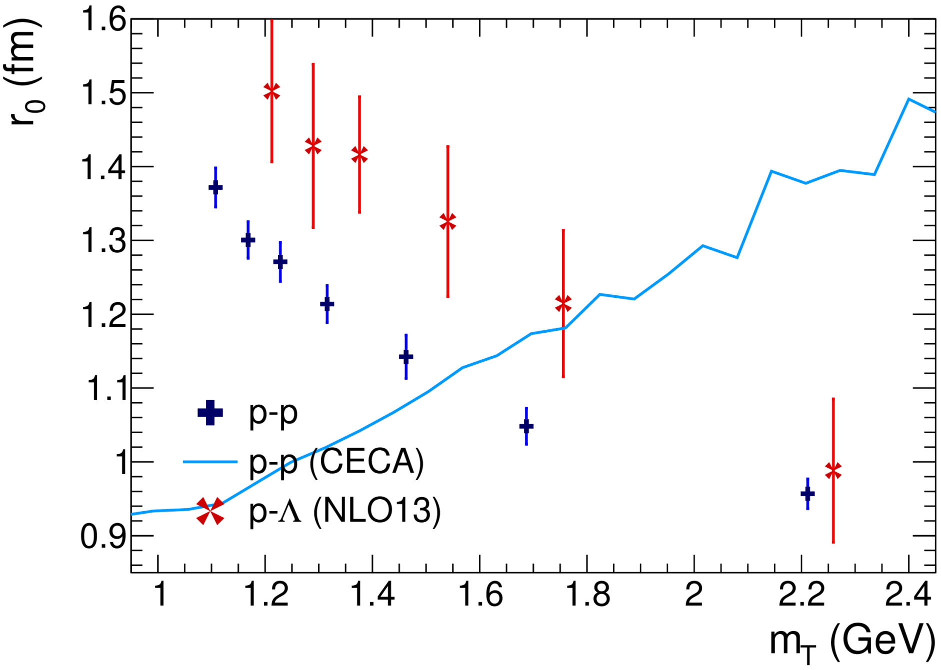

Figure 4.2: The effective source radius of p–p as a function of m_T (light blue), for a value of the displacement parameter of 1.0 fm, in comparison to the scaling from pp and pΛ from data [7].

reiterated several times to find the best match to the data. The manual work is required as a single evaluation of the source function, for a given set of parameters, lasts several minutes, whereas a fully automated fitter typically requires several thousand of function calls to converge. The result of this approach are the following values: 0.25 fm in the transversal plane and 0 fm in the beam direction for the displacement, 3.55 fm for the time offset and 2.3 fm in transversal and 0 fm in beam direction for the hadronization length. It has been observed that the source extension in the beam (z) direction has only a small effect, and it has been set to 0 arbitrarily. With this parameterization CECA is able to provide a perfect fit to the p–p m_T scaling, as seen in Figure 4.3. This indeed points to strong space-momentum correlations, as the random component of the source amounts to only 0.25 fm, which is comparable to the distribution of partons within the colliding protons. The resulting core and total source distributions at $m_T = 1.23$ GeV are shown in Fig. 4.4. They are both fitted with a Gaussian profile to extract the corresponding effective radii, which are $r_{\text{core}} = 0.48$ fm and $r_{\text{eff}} = 1.28$ fm. Both of the distributions deviate from a Gaussian profile, nevertheless, it has been verified that this does not introduce a

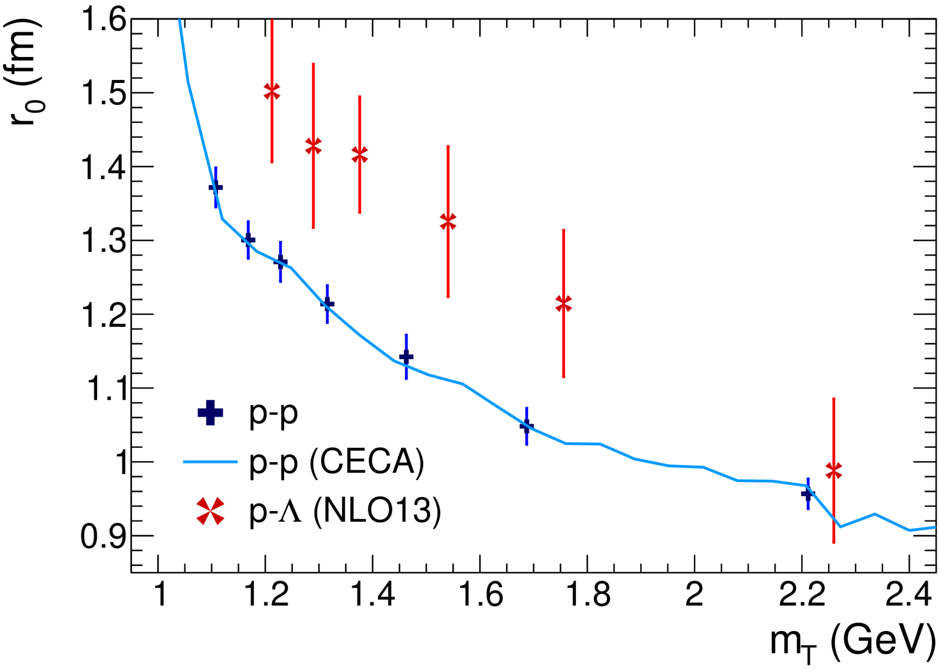

Figure 4.3: Scaling of the pp (blue) and pΛ (red) from the original analysis [7] with the p–p prediction of CECA (light blue), for the values of 0.25 fm for the displacement, 2.3 for the hadronization and 3.55 fm for the time offset.

great bias to the correlation function. Note that the total source distribution has a little bump at c.a. 1 fm, which corresponds to the emission of two primordial (core) protons, accounting for $\approx 12\%$ of all pairs. It has to be mentioned, that these parameters might not be a unique solution, and as a matter of fact, there is the possibility to completely leave out the displacement parameter out from the equation and set it to zero, which also provides a very good fit. It is possible to attempt to increase r_d and compensate its effect by increasing r_hl and decreasing τ_off, but the overall slope of the m_T starts to alter and becomes incompatible to the data at $r_\mathrm{d} \approx 0.4$ fm. Nevertheless, the next step is to predict the scaling of the p–Λ system, given the parameters obtained from p–p. This is done in order to test and reconfirm the hypothesis of a common emission source. The only changes that have to be made, are providing the momentum distribution of the Λ and the fraction of resonances, $P_\Lambda = 35.62\%$, including their average lifetime (4.69 fm), attained in the same way as for the protons.

This results in the scaling seen in Figure 4.5. What becomes apparent is that the prediction does not agree with the p–Λ measurement. On the positive side, the scaling is

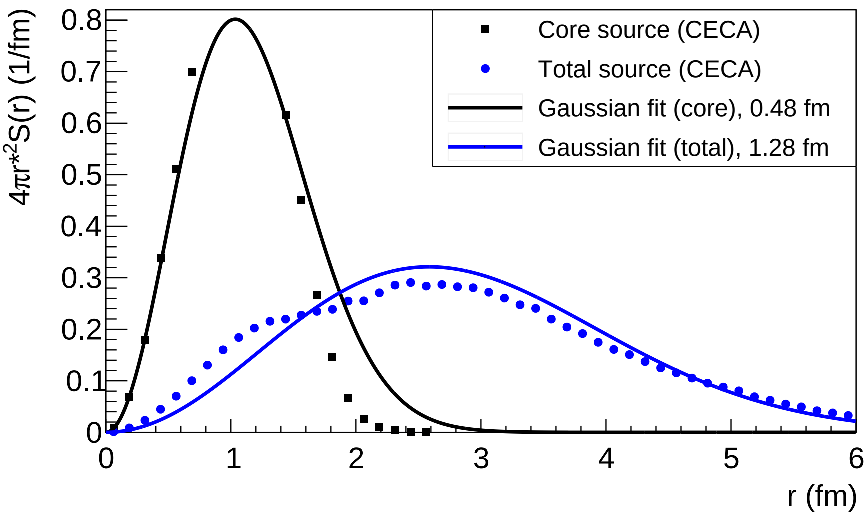

Figure 4.4: The core (black) and total (blue) p–p source from CECA, at m_T =1.23 GeV.

preserved and follows the trail of the data, which implies that the correlations introduced by CECA carry over when switching system. The discrepancy of the amplitude of the source is reconfirmed if the procedure is inverted, fixing the CECA parameters to p–Λ and transferring them to p–p (Fig. 4.6). This is actually to be expected, since the difference in the source sizes of the two systems only stems from the difference in the average lifetimes of the resonances, and not from the rest of the parameters. The following values describe the p–Λ system: $r_d = 0.2$ fm, $\tau_{off} = 3.85$ fm and $r_{hl} = 2.85$ fm.

These results seems to stand in contradiction to the assumption of a common source, since the effective radii provided by CECA match the p–p and p–Λ only if different primordial sources are assumed. However, there are alternative explanations, in particular that the p–Λ interaction is not accurately modeled, reflected in a systematic shift of the obtained source size. In Fig. 4.5 it can be seen that the CECA prediction is shifted to the edge of the experimental uncertainties, which are indeed dominated by the systematic component. Moreover, as discussed in section 4.1, the fits to the experimental correlations, used to create the p–Λ relation in Fig. 4.5 and in [7], are performed using either the LO or NLO13 tune of the chiral model, accounting only for the s-waves. This limitation enforced to fit $C(k^*)$ well below the NΣ cusp, located at $k^* = 289$ MeV/c, leading to a fit range between 0 and 228 MeV/c. This range does not allow for an accurate determination of the non-femtoscopic baseline, thus an additional bias might be present. Further, the analysis performed in [7] has been done with outdated assumptions regarding the feed-down contributions from p–Σ^0 and p–Ξ, whereas the subsequent dedicated p–Λ analysis [20] clearly shows their importance. All of these considerations lead to the decision of taking a deeper look at the p–Λ correlation function,

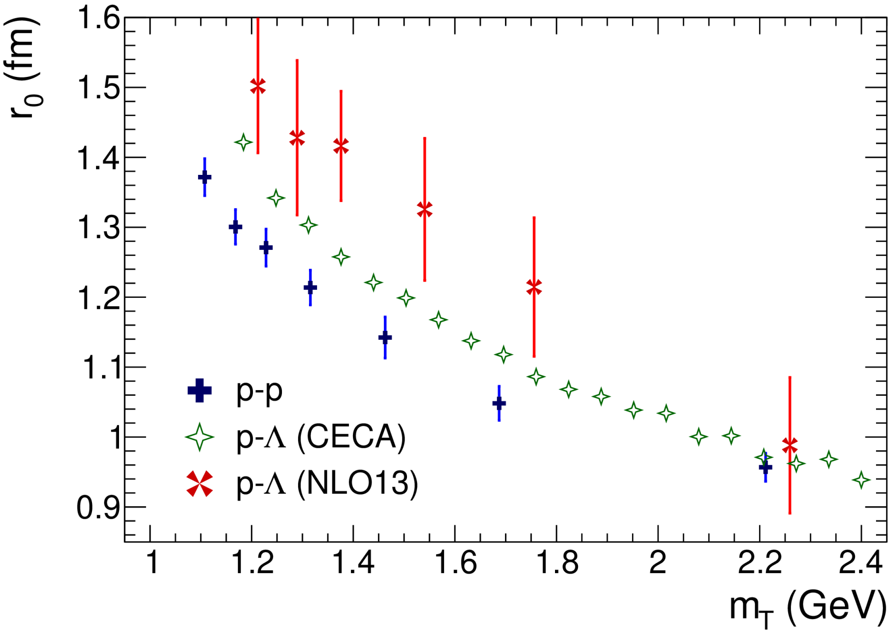

Figure 4.5: Effective source radius as a function of m_T for the p–p (blue) and p–Λ (red) system taken from [7] with the prediction of CECA (green) for the p–Λ, for the values of 0.25 fm for the displacement, 2.3 fm for the hadronization and 3.55 fm for the time offset.

and see how the updated analysis procedure influences the results on the source size. The work related to this analysis, and in particular [20], sparked a very useful private communication with the main author of the χEFT, Johann Haidenbauer, who provided a modified NLO19 calculation ($a_t = 1.41$ fm), in which the strength of the attraction in the 3S1 channel has been reduced to $a_t = 1.3$ fm. Such a modification is not contradicting the existing experimental constrains on p–Λ, and is thus of interest within the present analysis. Next, the measured p–Λ correlation functions [7] will have to be reanalyzed and refitted individually in m_T. This was possible, as my supervisor has been one of the analyzers of the ALICE results on p–Λ, and was able to provide me with the raw data corresponding to the published results. These already contain the fully reconstructed correlation functions.

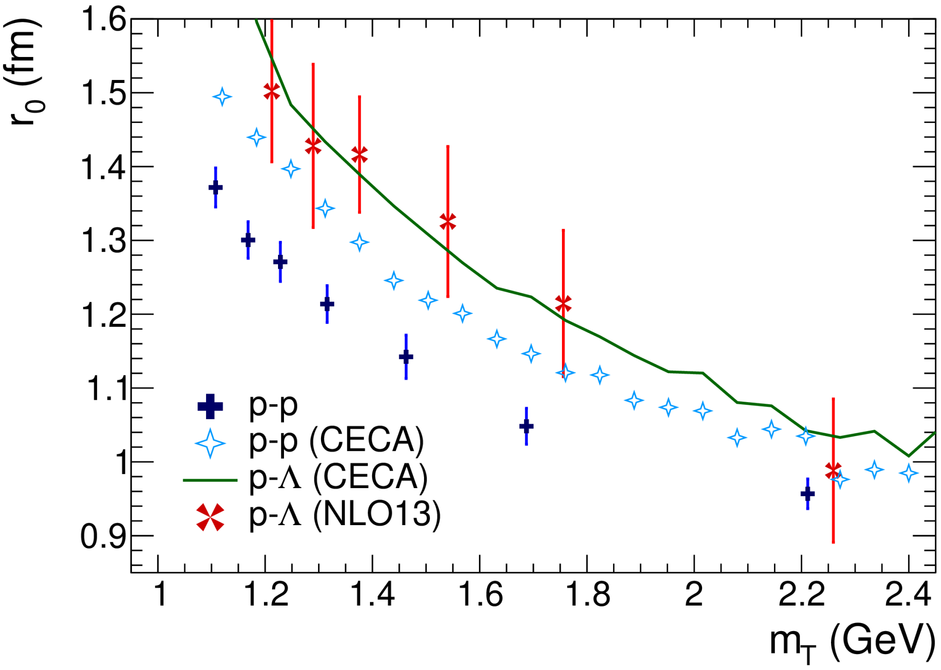

Figure 4.6: Effective source radius for the p–p (blue) and p–Λ (red) system taken from [7] with the prediction of CECA for the p–p (light blue), tuned to the pΛ scaling (green).

4.3 Refitting of the p–Λ correlation function

4.3.1 ALICE data

In the present work, the analysed correlation functions are obtained directly from the ALICE analysis related to the search of a common source [7]. For that reason the experimental details are omitted in the present manuscript, and this sub-section provides only the basics. For a detailed discussion of this topic refer to the PhD theses of either Dimitar Mihaylov [24] or Bernhard Hohlweger [32].

Both the p–p and p–Λ correlation functions have been measured by the ALICE experiment. It is located at the Large Hadron Collider (LHC), and the second data taking period (RUN2) of pp collisions at 13 TeV has been used in the present analysis. A schematic representation of the detector system is provided in Fig. 4.7. In a simplified picture, the single particle measurement of protons and Λs is performed as follows:

- Collide two protons at the center of ALICE, which is surrounded by a variety of

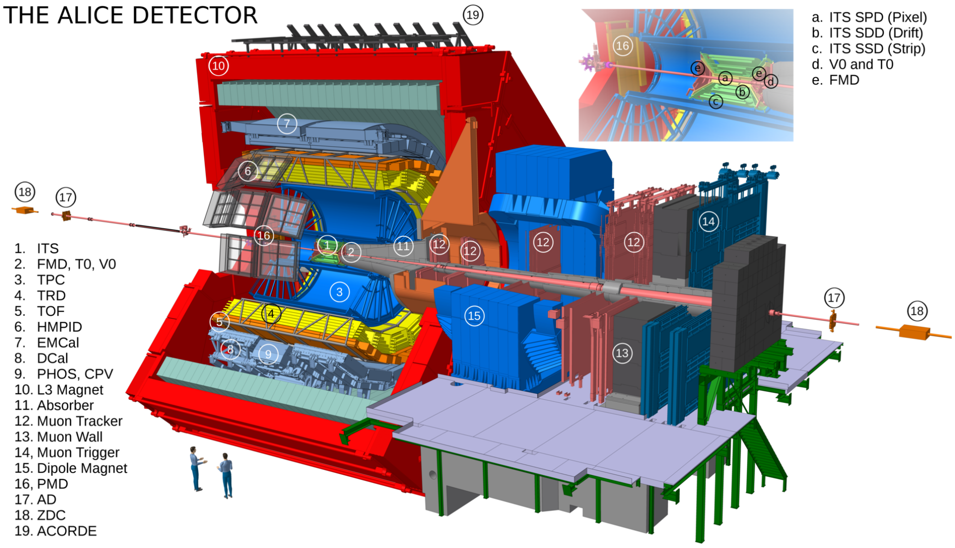

Figure 4.7: Schematic representation of the ALICE detector during the Run-2 data taking period (2015-2018) [33].

detector systems. The reconstructed collision point will be referred to as primary vertex (PV).

- Activate the detector read-out system, if a certain set of criteria are fulfilled (trigger). When the read-out is complete, the collected information is stored as an "event", and should correspond to a single collision. The basic trigger is called minimum-bias (MB) and it aims at introducing as little bias to the properties of the selected events as possible. In the current work a high-multiplicity (HM) data sample is used, where the triggering is performed only in events containing large amount of reconstructed charged particles (>30). This maximizes the probability of finding rare types of pairs, and is thus beneficial for femtoscopy.

- Within a single event, the charge particles first fly through the silicon based Inner Tracking System (ITS), and the generated signal allows to determine the trajectory (track) of the particles with high spacial resolution. Ultimately, this leads to a very accurate (<100 μm) determination of the PV.

- The charged particles then enter the huge Time Projection Chamber (TPC). This is a gas-filled detector, in which ionization happens when a charge particle traverses the volume. The generated electrons drift toward the two end-plates of the detector, and the signal is used to reconstruct (in 3D) the position (hit) of the particle. Due to the large size of the TPC, a single charged track can generate up to 159 hits, which are used to determine the trajectory. Since ALICE is surrounded by a very strong magnet, generating a field of strength 0.5 T, the charged particles fly on a curved trajectory, and the curvature allows to measure their momenta. On the other hand, the strength of the generated signal is related to the energy loss of the particles, which is connected to the velocity (Bethe-Bloch relation). The latter allows to disentangle the momentum and mass of the particles, leading to the identification of the particle species (PID). The TPC is crucial for femtoscopy measurements, as it allows for very accurate determination of both the momentum (<5% uncertainty) and the PID ($\approx 99\%$ purity for protons and pions).

- The Time of Flight (ToF) detector provides complementary information about the velocity of the particles, and boosts the PID capabilities for tracks of large momenta (>0.75 GeV/c). The main downside of ToF is the lowering of the reconstruction efficiency.
- The reconstruction of neutral particles, such as Λ, is done by using their charged decay products. For example, $\Lambda \rightarrow \mathrm{p}\pi$ with $c\tau = 7.89$ cm, allowing to measure the decay daughters. Thus, all measured $\mathrm{p}\pi$ pairs are investigated for a compatibility with a Λ decay, which is based on the combination of the $\mathrm{p}\pi$ invariant mass and the topological properties of the tracks.

After the particles of interest are reconstructed, each event is analyzed to search for p–Λ or $\overline{\mathrm{p}}$–$\overline{\Lambda}$ pairs, which exhibit the same FSI. The present analysis is performed with c.a. 10^9 events, leading to the detection of over $1.3 \cdot 10^6$ p–$\Lambda \oplus \overline{\mathrm{p}}$–$\overline{\Lambda}$ pairs with $\mathrm{k}^* < 200$ MeV/c. This large data sample allows to perform a differential analysis in 6 $\mathrm{m_T}$ bins, where the ranges of the bins are chosen such to result in an approximately equal pair yields. However, not all of these pairs represent the genuine p–Λ interaction (see chapter 2.2, Eq. 2.10). The topological selection of single particles is tuned to reconstruct predominantly primary particles, which stem either directly from the collision point (primordial) or are the decay products of short lived ($c\tau$ <<cm) resonances. These two scenarios cannot be separated by the detector, due to spacial resolution of the tracks. Nevertheless, the effect of the short lived resonances is included in the treatment of the source. By contrast, the topological selection helps to reduce the feed-down contribution from longer lived particles. However, these contributions are only partially suppressed, as tightening the selection criteria too much leads to a significant loss of signal. Nevertheless, it is possible to quantify the contribution of each feed-down channel, as the topological properties of the reconstructed tracks have different features. For example, the Distance of Closest Approach (DCA) of a track to the PV has a different underlying probability density function, based on the origin of the particle. Thus, a dedicated analysis of this distribution is capable to determine the amount of feed-down, using Monte-Carlo (MC) simulations. These ideas are thoroughly discussed and explained in [5, 24, 32]. In summary, the contributions considered within the correlation

Table 4.1: Weight parameters of the individual components of the p–Λ correlation function. The flat contributions include unaccounted feed-down and misidentifications. The default values correspond to the analysis [20], while the values in square brackets correspond to [7]. In the latter (older) analysis, the p–Ξ^0 contribution has been treated as effectively flat. The two last rows correspond to the values of the λ parameters within the systematic variations.

Pair	$\mathrm{p}\Lambda$	$\mathrm{p}(\Sigma^0)$	$\mathrm{p}(\Xi^-)$	$\mathrm{p}(\Xi^0)$	Flat
λ_{Pair} (%)	45.4 [45.2]	15.1 [15.1]	9.1 [9.1]	9.1 [n/a]	21.2 [30.6]
min{λ_{Pair}} (%)	40.7 [43.1]	12.0 [12.7]	9.0 [7.3]	9.0 [n/a]	21.2 [28.8]
max{λ_{Pair}} (%)	47.8 [47.6]	17.3 [17.2]	10.7 [10.9]	10.7 [n/a]	22.0 [32.4]

function in this analysis are listed in Table 4.1. The particles enclosed in brackets represent feed-down contributions, e.g. $\mathrm{p}(\Sigma^0)$ is the amount of residual p–Σ^0 signal seen in p–Λ. Since the present work will be compared to both ALICE works involving the p–Λ correlation [7, 20], and the two analyses have minor differences[1], two different sets of λ parameters will be used. Further, small transformations are performed to accommodate the differences to the present analysis, e.g. the dedicated p–Λ paper [20] works with an unfolded data set corrected for the impurities of the Λ, while this is not done here, hence a minor modification to the decomposition is required. Ultimately, the total correlation function is:

$$C_{\text{tot}}(k^*) = \lambda_{\mathrm{p}\Lambda} \cdot C_{\mathrm{p}\Lambda}(k^*) + \lambda_{\mathrm{p}(\Sigma^0)} C_{\mathrm{p}(\Sigma^0)} + \lambda_{\mathrm{p}(\Xi^-)} C_{\mathrm{p}(\Xi^-)} + \lambda_{\mathrm{p}(\Xi^0)} C_{\mathrm{p}(\Xi^0)} + \lambda_{\text{flat}}. \quad (4.1)$$

The flat component includes both the flat feed-down, as well as the contribution related to misidentified particles. The rest of the feed-down correlation functions are computed exactly as described in either [7] or [20], depending on the tested scenario. The latter is a more recent paper, hence the analysis has evolved, and can overall be considered more accurate.

4.3.2 Analysis of the correlations

The development of CECA is still ongoing, and using its source function directly in CATS is currently not very practical. To simplify the present analysis, the source function used to fit the p–Λ correlations is Gaussian (Eq. 2.8), while any comparisons to CECA will be performed by using an effective Gaussian source size provided by the model, following the procedure explained in section 4.2. In essence, the goal is to reproduce Fig. 4.5, by

[1] The underlying data is the same, however the analysis techniques have been improved in [20], leading to minor differences.

fitting the corresponding p–Λ correlations using a Gaussian source, but adopting different settings regarding the fitter and testing several wave functions. This will demonstrate if the prediction of CECA (green points in Fig. 4.5) correspond to a reasonably small modification of the p–Λ interaction, and can thus be considered realistic. The following scenarios will be tested:

I. Fit the correlation functions with exactly the same settings as used in the ALICE paper on the emission source [7]. This is done to ensure that the code implemented within this work is compatible with the original code used for the ALICE publication. Here the NLO13 s-wave wave function has been used.

II. Fit the correlation functions using the settings from the dedicated ALICE p–Λ paper [20]. The main difference is the usage of the NLO19 parameterization of the chiral theory, including both s- and d-waves to properly model the coupling to NΣ. This allows to extend the fit range to and above the NΣ cusp, making possible to better constrain the non-femtoscopic baseline. There are several further refinements, compared to the older analysis [7], such as an improved modeling of the p–Σ^0 and p–Ξ feed-down.

III. One of the conclusions done in [20] is that a weaker two-body p–Λ attraction in vacuum is preferred by the ALICE data. This statement is based on the preference of NLO19 over NLO13. Moreover, the final fit quality, using NLO19, is still not satisfactory, thus in the present work the hypothesis of even lower attraction is tested. This is achieved[2] by reducing the strength of the interaction within the triplet channel by almost 10%.

Following the analysis procedures described in both ALICE papers [7, 20] the systematic uncertainties of the fit have been included by repeating the fit multiple times, in each random sampling several parameters. The "topological" variations are related to the reconstruction procedure, and account for creating 43 distinct correlation functions, each corresponding to a random modification of the topological criteria within some set limits. As mentioned, details can be found in the theses of D. Mihaylov and B. Hohlweger [24, 32]. Within the present work these have been included by selecting one of these 43 correlation functions, randomly, in each systematic variation. Next is the variation of the fit range, where the upper limit is chosen randomly from 3 predefined values. These are 204, 228 and 240 MeV/c for scenario (I), and 432, 456 and 480 MeV/c for scenarios (II) and (III). For the first scenario (I) the baseline hypothesis is randomly selected between a constant factor and a linear function. For the updated scenarios (II) and (III) the baseline is fixed as a polynomial of third degree (Eq. 2.11). There are two further variations, the values of the λ parameters (see Table 4.1) and the expected production ratio of Σ:Λ, which is important for fixing the strength of the cusp [20, 24]. The latter has been varied

[2]Work of Johann Haidenbauer, done within the scope of private communication.

within $1/3 \pm 20\%$. This is based on the expectation considering the isospin degeneracy, as Λ is I=0 (singlet) and Σ is I=1 (triplet). This implies that assuming a similar amount of Λ and Σ production, each individual Σ state is only 1/3 probable compared to Λ. As explained in section 2.2, the non-femtoscopic correlations are taken care of with a polynomial BL function (2.11), which serves as a correction term for the total correlation function as seen in eq. 2.12. Additionally, due to the presence of strong long-range effects, the femtoscopic correlations cannot be reliably normalized and the constant $\mathcal{N}$ is left free as well. Ultimately the following fit function is used:

$$C_{\text{model}}(k^*) = \mathcal{N}(1 + p_2 \cdot k^{*2} + p_3 \cdot k^{*3}) \cdot C_{\text{tot}}(k^*). \tag{4.2}$$

The femtoscopic signal $C_{\text{tot}}(k^*)$ is evaluated with CATS, where the parameters from the BL are left free. The source function is assumed to be a Gaussian profile and lastly, the p–Λ interaction is modeled using the different chiral potentials (see section 4.1).

First, the same settings for the variations are used, as was done in the analysis of the source function in [7], with the NLO13, to show the equivalence of the two models (scenario I). Once again, the fit is done individually for each m_T bin and two example fits are shown in Fig. 4.8. The top (middle) panel shows the correlation function (zoomed), while the bottom panel shows the deviation between data and theory given in

$$n_\sigma = \frac{\text{data} - \text{theory}}{\text{uncertainty}} \tag{4.3}$$

and evaluated in each k^* bin. This observable is the building block of the χ^2, where the ratio of the deviation of the data from the theory to the uncertainty is squared, and provides a measurable value for the fit accuracy. The χ^2 is defined as

$$\chi^2 = \sum_i^{\text{entries}} \left[\frac{\text{data}_i - \text{theory}_i}{\text{uncertainty}_i}\right]^2. \tag{4.4}$$

Further description on the χ^2 can be read in [24]. Overall the fit quality deteriorates at low k^* and large m_T, but is quite good for low m_T. The extracted Gaussian source size r_0 is plotted in Fig. 4.9, where the original ALICE result is shown for comparison. Clearly the two relations are identical, up to negligible fluctuations well below the uncertainty. This implies that the framework developed within the present thesis delivers an output consistent with the original ALICE analysis, and can be trusted to re-evaluate the results using a different set-up for the interaction and an extended fit range (scenarios II and III). The results for scenario II, which uses the NLO19 potential and the updated analysis procedure following [20], are shown in Fig. 4.10 (fits) and Fig. 4.11 ($r_0(m_T)$). The quality of the fits is better, in particular for large m_T, while the overall extracted source size decreases a little bit. This is attributed to the inclusion of d-waves into the model, extending the fit range in consequence, and the slightly lower two-body attraction within

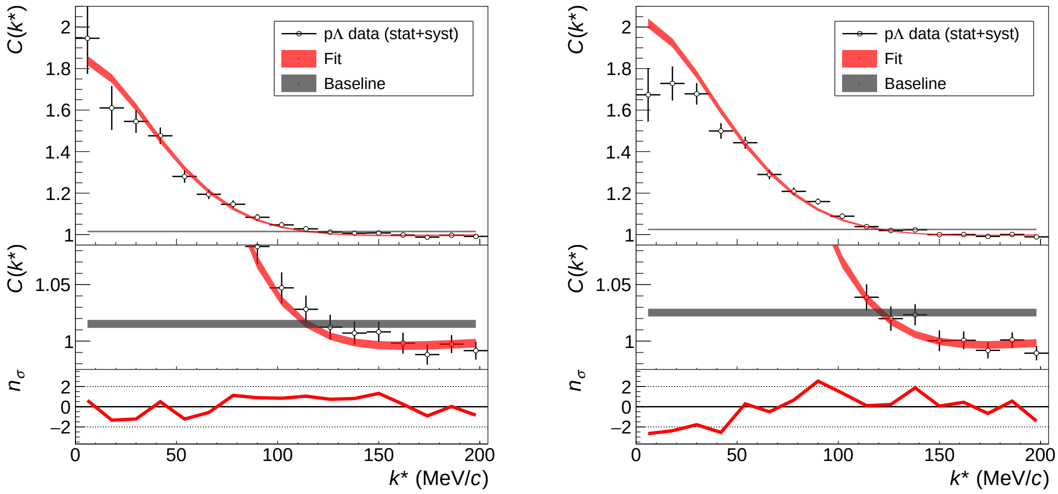

Figure 4.8: $C(k^*)$ (black points) for the p–Λ system in the 2nd (left) and 5th (right) m_T bin with the NLO13 potential, using the limited fit range as in [7] (scenario I).

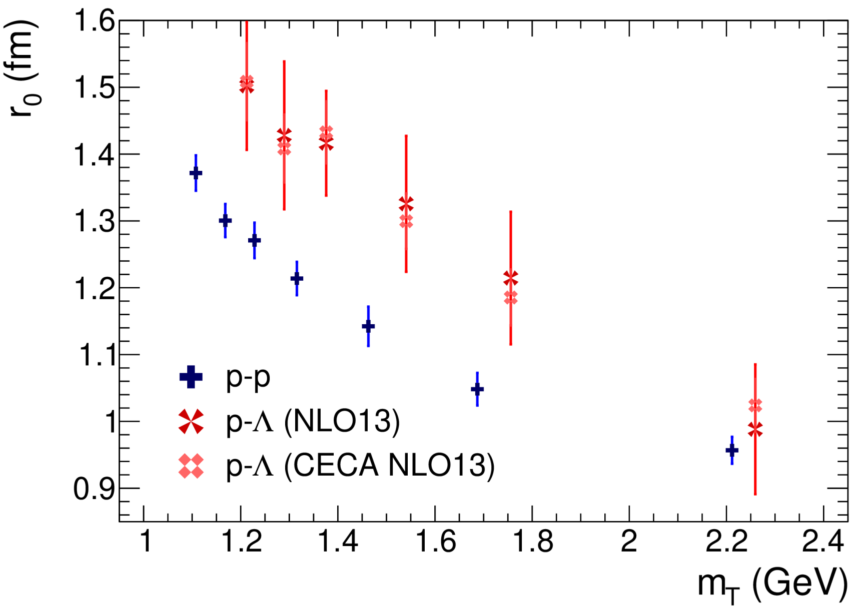

Figure 4.9: Effective radii for the p–p and the p–Λ system, where the modeling of the p–Λ was performed with CECA (light red) and with the RSM (dark red) for the NLO13 potential.

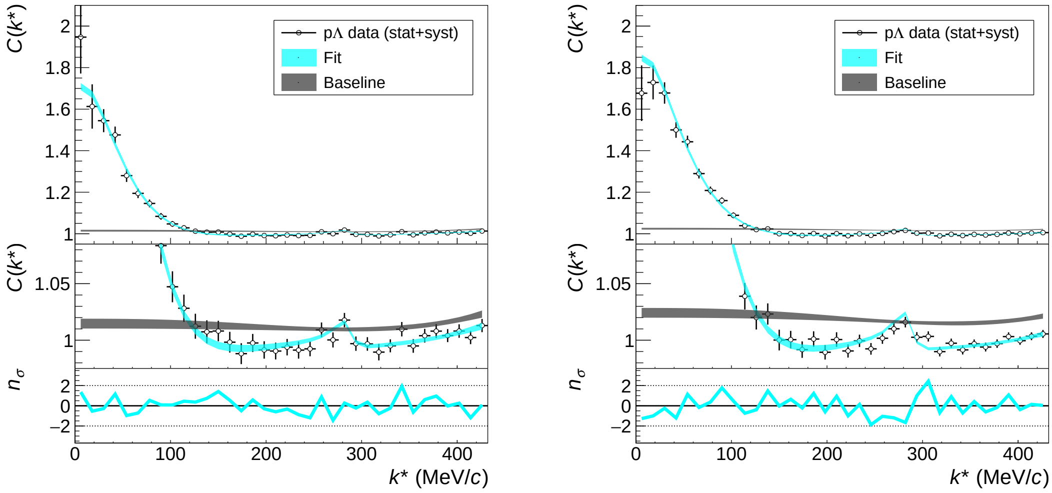

Figure 4.10: $C(k^*)$ (black points) for the p–Λ system in the 2nd (left) and 5th (right) m_T bin with the NLO19 potential, using the extended fit range as in [20] (scenario II).

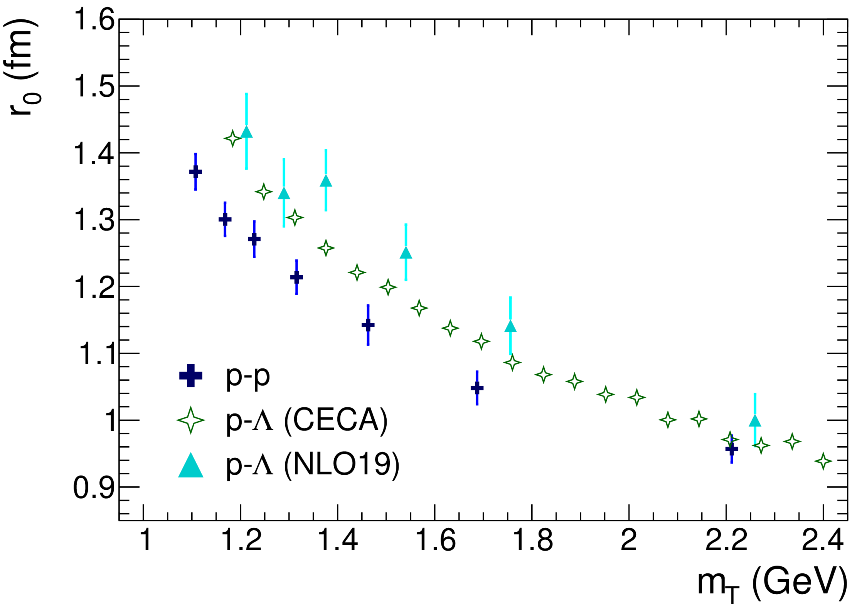

Figure 4.11: Effective radii of the p–p and the p–Λ (NLO19) system alongside the prediction of CECA for the p–Λ system (green).

the NLO19 parameterization. The discrepancy to the CECA prediction is reduced, nevertheless a slight systematic bias is still present. The reason for this persistent discrepancy is not yet completely clear, as it may be attributed to either the interaction or remaining inaccuracies in the modeling of the source. Nevertheless, one further test was performed, in which the hypothesis of a lower strength of the two-body attraction is assumed. This corresponds to scenario III, and the results are shown in Figs. 4.12 and 4.13. It leads to an expectation of even smaller source size, compared to II. The quality of the fits is good and very similar to the previous case (NLO19), while the $r_0(m_T)$ relation is essentially compatible with the CECA prediction. The figures for the rest of the m_T bins can be found in the appendix.

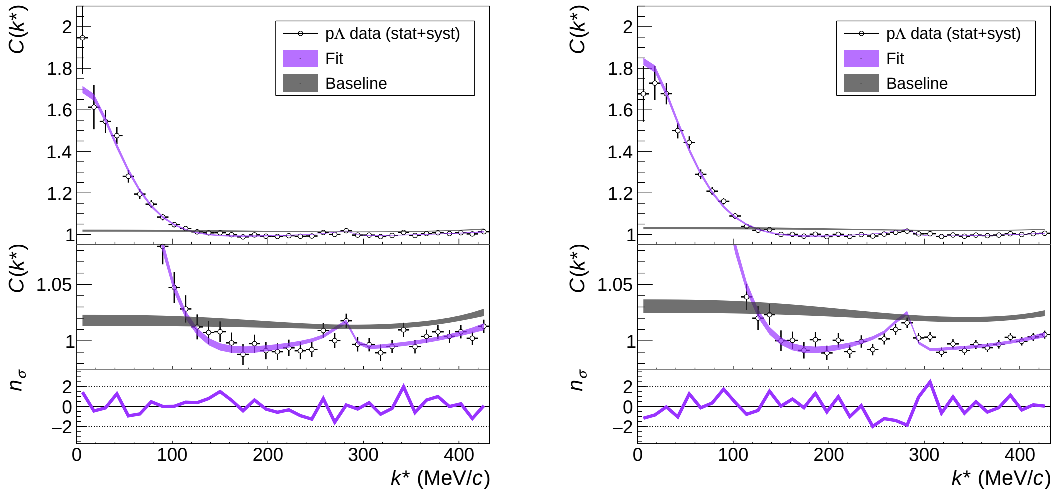

Figure 4.12: $C(k^*)$ (black points) for the p–Λ system in the 2nd (left) and 5th (right) m_T bin with the NLO19 potential with reduced two-body attraction, using the extended fit range as in [20] (scenario III).

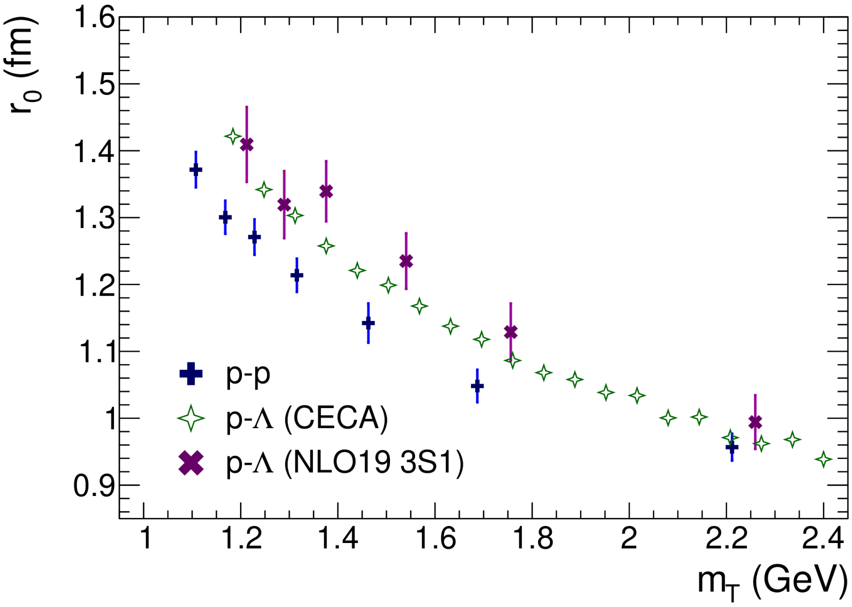

Figure 4.13: Effective radii of the p–p and the p–Λ system alongside the prediction of CECA for the p–Λ system (green). The interaction potential for the p–Λ is a modified version of the NLO19 with a reduced scattering length for the 3S1 channel.

4.4 Discussion

The modeling of the emission source in femtoscopy is very important to understand the details of the interaction between pairs of particles. Small collision systems are expected to posses a common source for all particle species, baryons in particular, allowing to fix the emission source based on a system of known interaction, such as p–p. The validity of this concept has been demonstrated by the ALICE collaboration for protons and Λ hyperons, by developing the Resonance Source Model, which corrects the emission source for the effect of particle production through short lived resonances. This model had certain shortcomings, that motivated an upgrade and lead to the development of a new framework to model the source, CECA, which was presented in this work. It is more generic to its predecessor, due to the modeling of the two-body source based on single particle properties. The effects of short lived resonances are again included, but in addition it is possible to correlate the space and momentum coordinates of each particle, mimicking the effect of collectively, leading to an $\mathrm{m_T}$ scaling of the source size. This was previously not properly modeled.

Within the present work, CECA was tested for the first time. The initial part of the performed analysis was to fine tune three of the parameters within the model, in order to reproduce the ALICE results on the $\mathrm{m_T}$ scaling of the p–p system. This was successfully achieved. Further, assuming a common emission for all particles, the p–Λ source size was estimated with CECA. It was shown that the CECA prediction laid below the published ALICE results on the p–Λ emission source, even though the $\mathrm{m_T}$ scaling was qualitatively reproduced. These ALICE results were obtained using the χEFT to model the p–Λ interaction, but only accounting for the s-wave. In a newer dedicated ALICE study, it was demonstrated that the inclusion of d-waves is essential to capture the details related to the $\mathrm{N\Sigma} \leftrightarrow \mathrm{N\Lambda}$ coupled channel. The same study argues that a lower two-body attraction, which is allowed within the existing experimental constraints, is preferred by the femtoscopic measurements. In this thesis, the ALICE $\mathrm{m_T}$ differential data on the p–Λ correlation were re-analyzed using the state-of-the-art techniques and interaction models. With the assistance of the main author of the chiral model, it was possible to test the hypothesis of a reduced attraction in the S=1 p–Λ channel. It was shown that these improvements for the modeling of the p–Λ correlation lead to a lowering of the source size, making the ALICE results fully compatible with the CECA prediction.

This observation preserves the idea of a common emission source for all baryons, and hints at a possible overestimated two-body p–Λ attraction within the χEFT. For the future, it will be very important to analyse the source of meson–meson or baryon–meson pairs, using CECA, in order to fully validate the model. If done successfully, this will increase the precision to which femtoscopy can be used to study the strong force, as it will remove one of the main sources of systematic bias in these types of studies. For example, based on the findings within the present work, the physics message related to the p–Λ interaction will strengthen, implying a lower two-body attraction over the currently accepted values.

Consequently, this will help construct a more realistic nuclear Equation of State and lead to a better understanding of the structure of neutron stars. Such exotic studies are to be accompanied by measurements of the three body nucleon–nucleon–hyperon correlations, and the CECA framework will be the key to model the three-body source.

Appendix A

p_T distributions and $C(k^*)$ graphs

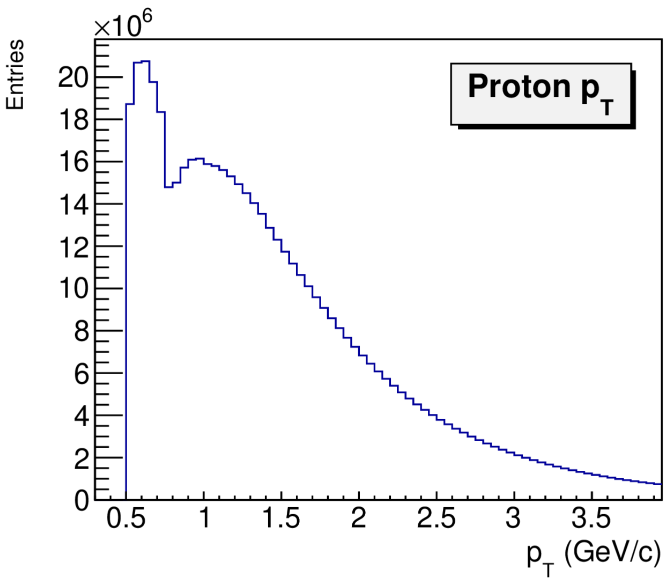

Figure A.1: Transversal momentum distribution of the proton.

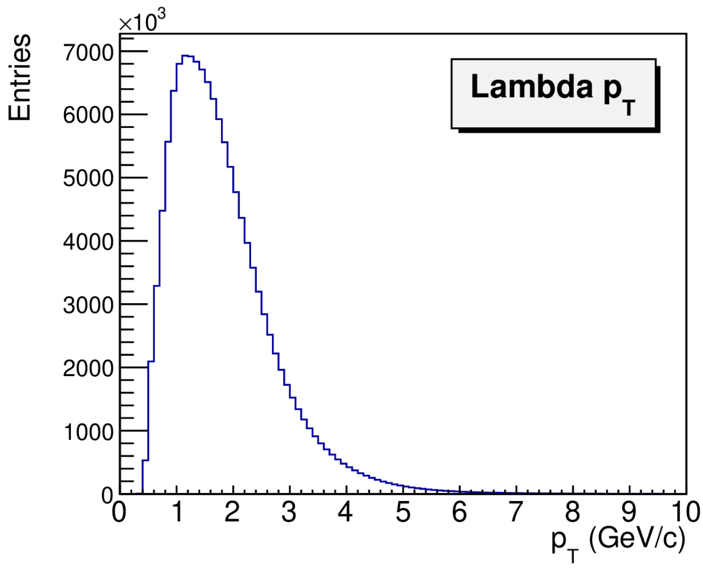

Figure A.2: Transversal momentum distribution of the Λ.

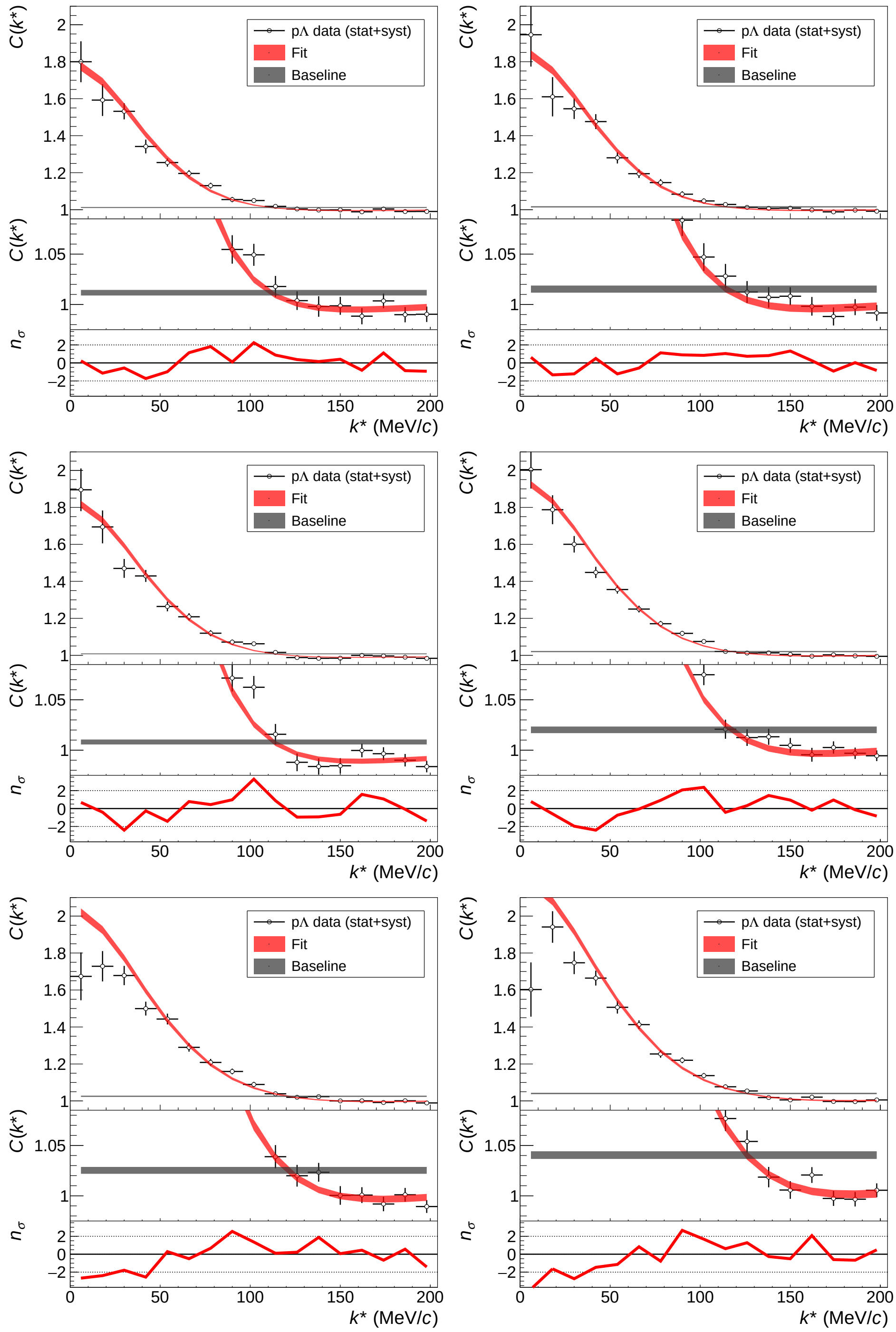

Figure A.3: $C(k^*)$ of the p–Λ system for the m_T bins with the NLO13 potential.

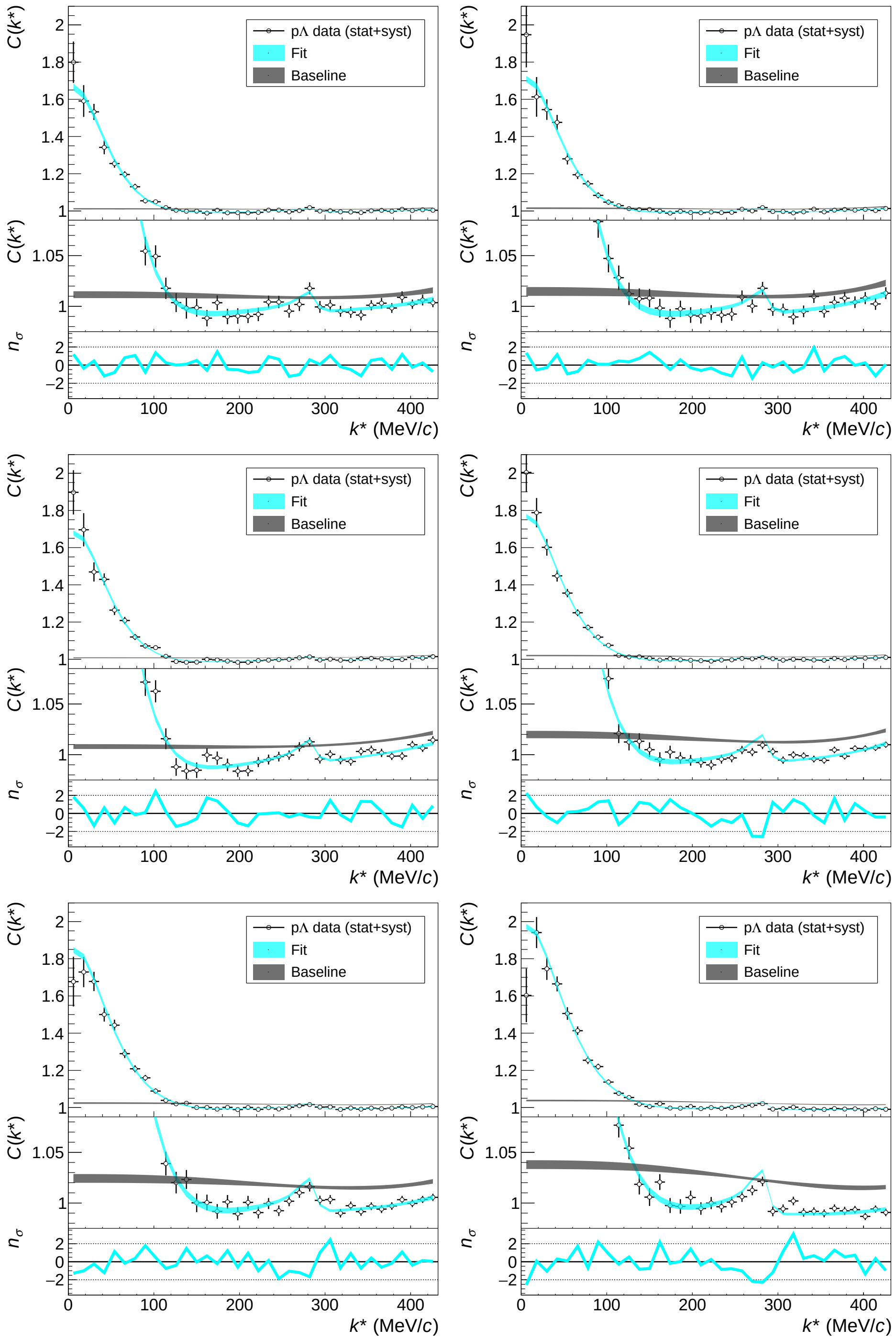

Figure A.4: $\mathrm{C}(\mathrm{k}^*)$ of the p–Λ system for the m_{T} bins with the NLO19 potential.

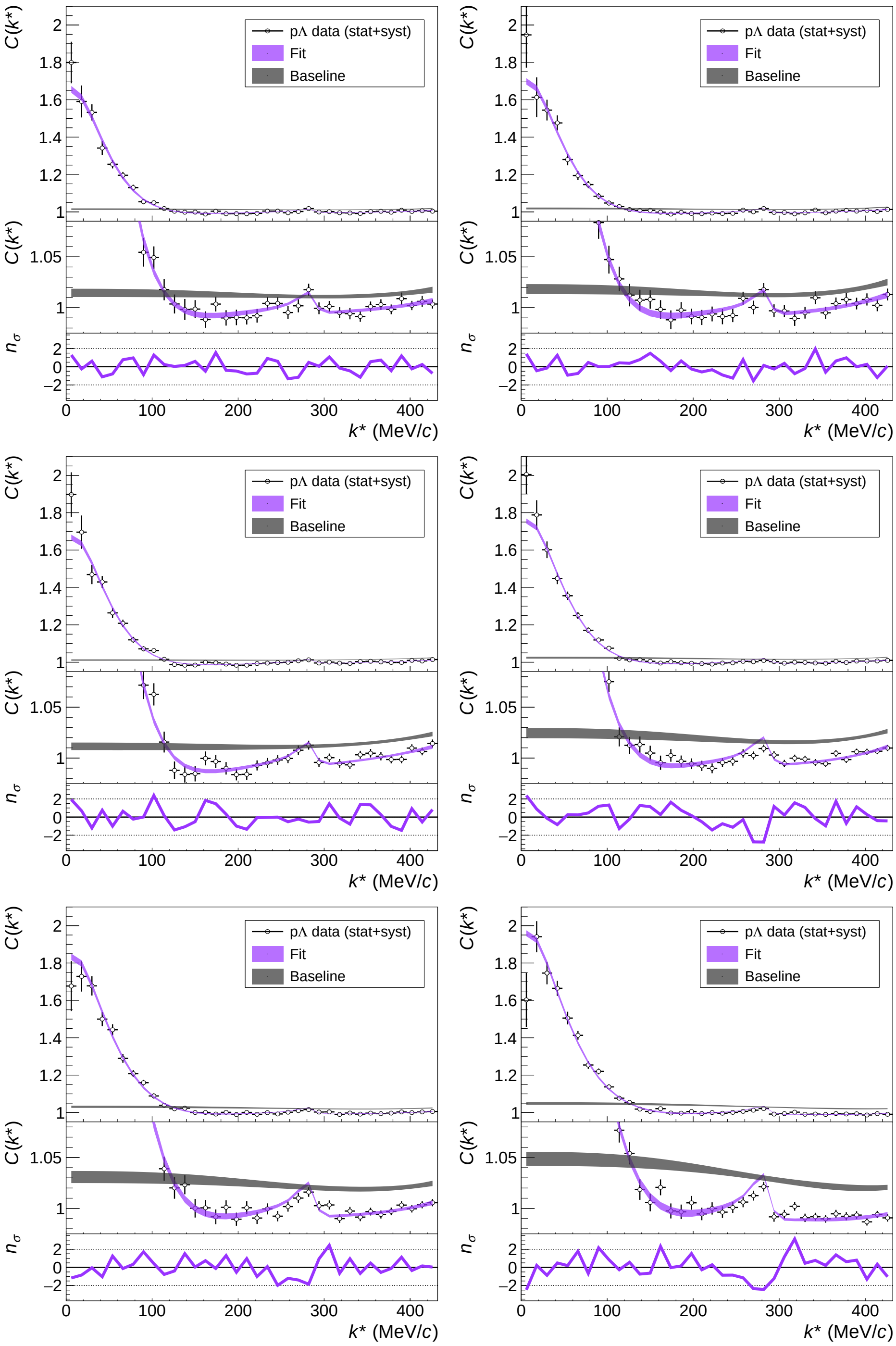

Figure A.5: $C(k^*)$ of the p–Λ system for all m_T bins with the NLO19 3S1 potential.

Bibliography

[1] J. Haidenbauer et al. 'Hyperon-nucleon interaction at next-to-leading order in chiral effective field theory'. In: *Nucl. Phys. A* 915 (2013), pp. 24–58. DOI: 10.1016/j.nuclphysa.2013.06.008. arXiv: 1304.5339 [nucl-th] (cit. on pp. 1, 23).

[2] J. Haidenbauer, U.-G. Meißner and A. Nogga. 'Hyperon–nucleon interaction within chiral effective field theory revisited'. In: *The European Physical Journal A* 56.3 (Mar. 2020). DOI: 10.1140/epja/s10050-020-00100-4. URL: https://doi.org/10.1140%2Fepja%2Fs10050-020-00100-4 (cit. on pp. 1, 7, 23).

[3] Jürgen Schaffner-Bielich. *Compact Star Physics*. Cambridge University Press, 2020. ISBN: 978-1107180895 (cit. on p. 1).

[4] Diego Lonardoni et al. 'Hyperon Puzzle: Hints from Quantum Monte Carlo Calculations'. In: *Phys. Rev. Lett.* 114.9 (2015), p. 092301. DOI: 10.1103/PhysRevLett.114.092301. arXiv: 1407.4448 [nucl-th] (cit. on p. 2).

[5] Shreyasi Acharya et al. 'p-p, p-Λ and Λ-Λ correlations studied via femtoscopy in pp reactions at $\sqrt{s} = 7$ TeV'. In: *Phys. Rev. C* 99.2 (2019), p. 024001. DOI: 10.1103/PhysRevC.99.024001. arXiv: 1805.12455 [nucl-ex] (cit. on pp. 2, 3, 6, 9, 13, 33).

[6] Alice Collaboration et al. 'Unveiling the strong interaction among hadrons at the LHC'. In: *Nature* 588 (2020). [Erratum: Nature 590, E13 (2021)], pp. 232–238. DOI: 10.1038/s41586-020-3001-6. arXiv: 2005.11495 [nucl-ex] (cit. on pp. 2, 3, 13).

[7] Shreyasi Acharya et al. 'Search for a common baryon source in high-multiplicity pp collisions at the LHC'. In: *Phys. Lett. B* 811 (2020), p. 135849. DOI: 10.1016/j.physletb.2020.135849. arXiv: 2004.08018 [nucl-ex] (cit. on pp. 2–4, 7, 9, 12–16, 19, 23–25, 27–31, 34–37).

[8] R. Hanbury Brown and R.Q. Twiss. 'A Test of a new type of stellar interferometer on Sirius'. In: *Nature* 178 (1956), pp. 1046–1048. DOI: 10.1038/1781046a0 (cit. on p. 3).

[9] Gordon Baym. 'The Physics of Hanbury Brown-Twiss intensity interferometry: From stars to nuclear collisions'. In: *Acta Phys. Polon. B* 29 (1998). Ed. by A. Bialas, pp. 1839–1884. arXiv: `nucl-th/9804026` (cit. on p. 3).

[10] Michael Annan Lisa et al. 'FEMTOSCOPY IN RELATIVISTIC HEAVY ION COLLISIONS: Two Decades of Progress'. In: *Annual Review of Nuclear and Particle Science* 55.1 (Dec. 2005), pp. 357–402. DOI: `10.1146/annurev.nucl.55.090704.151533`. URL: `https://doi.org/10.1146%2Fannurev.nucl.55.090704.151533` (cit. on pp. 3, 5, 12, 18).

[11] Gerson Goldhaber et al. 'Influence of Bose-Einstein statistics on the anti-proton proton annihilation process'. In: *Phys. Rev.* 120 (1960). Ed. by R.M. Weiner, pp. 300–312. DOI: `10.1103/PhysRev.120.300` (cit. on p. 3).

[12] R. Lednicky and V. L. Lyuboshits. 'Final State Interaction Effect on Pairing Correlations Between Particles with Small Relative Momenta'. In: *Yad. Fiz.* 35 (1981), pp. 1316–1330 (cit. on pp. 3, 10).

[13] Shreyasi Acharya et al. 'First study of the two-body scattering involving charm hadrons'. In: *Phys. Rev. D* 106.5 (2022), p. 052010. DOI: `10.1103/PhysRevD.106.052010`. arXiv: `2201.05352 [nucl-ex]` (cit. on pp. 3, 13).

[14] 'First measurement of the Λ-Ξ interaction in proton-proton collisions at the LHC'. In: (Apr. 2022). DOI: `10.1016/j.physletb.2022.137223`. arXiv: `2204.10258 [nucl-ex]` (cit. on pp. 3, 13).

[15] Shreyasi Acharya et al. 'Study of the Λ-Λ interaction with femtoscopy correlations in pp and p-Pb collisions at the LHC'. In: *Phys. Lett. B* 797 (2019), p. 134822. DOI: `10.1016/j.physletb.2019.134822`. arXiv: `1905.07209 [nucl-ex]` (cit. on pp. 3, 13).

[16] Shreyasi Acharya et al. 'First Observation of an Attractive Interaction between a Proton and a Cascade Baryon'. In: *Phys. Rev. Lett.* 123.11 (2019), p. 112002. DOI: `10.1103/PhysRevLett.123.112002`. arXiv: `1904.12198 [nucl-ex]` (cit. on pp. 3, 13).

[17] Shreyasi Acharya et al. 'Investigation of the p–Σ0 interaction via femtoscopy in pp collisions'. In: *Phys. Lett. B* 805 (2020), p. 135419. DOI: `10.1016/j.physletb.2020.135419`. arXiv: `1910.14407 [nucl-ex]` (cit. on pp. 3, 13).

[18] 'Experimental Evidence for an Attractive p-ϕ Interaction'. In: *Phys. Rev. Lett.* 127.17 (2021), p. 172301. DOI: `10.1103/PhysRevLett.127.172301`. arXiv: `2105.05578 [nucl-ex]` (cit. on pp. 3, 13).

[19] Shreyasi Acharya et al. 'Investigating the role of strangeness in baryon–antibaryon annihilation at the LHC'. In: *Phys. Lett. B* 829 (2022), p. 137060. DOI: `10.1016/j.physletb.2022.137060`. arXiv: `2105.05190 [nucl-ex]` (cit. on pp. 3, 13).

[20] Shreyasi Acharya et al. ‘Exploring the NΛ–NΣ coupled system with high precision correlation techniques at the LHC’. In: *Phys. Lett. B* 833 (2022), p. 137272. DOI: 10.1016/j.physletb.2022.137272. arXiv: 2104.04427 [nucl-ex] (cit. on pp. 3, 10, 13, 23–25, 29, 30, 34–36, 38, 40).

[21] D. L. Mihaylov et al. ‘A femtoscopic correlation analysis tool using the Schrödinger equation (CATS)’. In: *The European Physical Journal C* 78.5 (May 2018). DOI: 10.1140/epjc/s10052-018-5859-0. URL: https://doi.org/10.1140%2Fepjc%2Fs10052-018-5859-0 (cit. on pp. 3, 11, 15, 23).

[22] Robert B. Wiringa, V.G.J. Stoks and R. Schiavilla. ‘An Accurate nucleon-nucleon potential with charge independence breaking’. In: *Phys. Rev. C* 51 (1995), pp. 38–51. DOI: 10.1103/PhysRevC.51.38. arXiv: nucl-th/9408016 (cit. on p. 7).

[23] Henk Polinder, Johann Haidenbauer and Ulf-G. Meißner. ‘Hyperon–nucleon interactions—a chiral effective field theory approach’. In: *Nuclear Physics A* 779 (Nov. 2006), pp. 244–266. DOI: 10.1016/j.nuclphysa.2006.09.006. URL: https://doi.org/10.1016%2Fj.nuclphysa.2006.09.006 (cit. on pp. 7, 23).

[24] Dimitar Mihaylov. ‘Analysis techniques for femtoscopy and correlation studies in small collision systems and their applications to the investigation of p–Λ and Λ–Λ interactions with ALICE’. In: *PhD thesis, Technical University of Munich* (2021) (cit. on pp. 9, 11, 25, 31, 33, 35, 36).

[25] David Griffiths. *Introduction to Quantum Mechanics*. Pearson Prentice Hall, 2004. ISBN: 978-1107179868 (cit. on p. 11).

[26] T. Pierog et al. ‘EPOS LHC: Test of collective hadronization with data measured at the CERN Large Hadron Collider’. In: *Phys. Rev. C* 92.3 (2015), p. 034906. DOI: 10.1103/PhysRevC.92.034906. arXiv: 1306.0121 [hep-ph] (cit. on pp. 13, 15).

[27] F Becattini et al. ‘Predictions of hadron abundances in *pp* collisions at the LHC’. In: *Journal of Physics G: Nuclear and Particle Physics* 38.2 (Jan. 2011), p. 025002. DOI: 10.1088/0954-3899/38/2/025002. URL: https://doi.org/10.1088%2F0954-3899%2F38%2F2%2F025002 (cit. on pp. 13, 15).

[28] O. Hashimoto and H. Tamura. ‘Spectroscopy of Lambda hypernuclei’. In: *Prog. Part. Nucl. Phys.* 57 (2006), pp. 564–653. DOI: 10.1016/j.ppnp.2005.07.001 (cit. on p. 23).

[29] A. Gal, E. V. Hungerford and D. J. Millener. ‘Strangeness in nuclear physics’. In: *Rev. Mod. Phys.* 88 (2016), p. 035004. DOI: 10.1103/RevModPhys.88.035004. arXiv: 1605.00557 [nucl-th] (cit. on p. 23).

[30] Dominik Gerstung, Norbert Kaiser and Wolfram Weise. 'Hyperon–nucleon three-body forces and strangeness in neutron stars'. In: *Eur. Phys. J. A* 56.6 (2020), p. 175. DOI: 10.1140/epja/s10050-020-00180-2. arXiv: 2001.10563 [nucl-th] (cit. on p. 24).

[31] 'Towards the understanding of the genuine three-body interaction for p—p—p and p—p—Λ'. In: (June 2022). arXiv: 2206.03344 [nucl-ex] (cit. on p. 24).

[32] Bernhard Hohlweger. 'First observation of the p–Ξ^- interaction via two-particle correlations'. In: *PhD thesis, Technical University of Munich* (2020) (cit. on pp. 25, 31, 33, 35).

[33] ALICE Collaboration. 'ALICE Figure repository'. In: *Accessed 4th December 2020* () (cit. on p. 32).